GEOSPHERE

GEOSPHERE, v. 16, no. 3

https://doi.org/10.1130/GES02227.1

11 figures; 2 tables; 1 set of supplemental files

CORRESPONDENCE:
jesus.munozmontecinos@gmail.com

CITATION: Muñoz-Montecinos, J., Angiboust, S., Cambeses, A., and García-Casco, A., 2020, Multiple veining in a paleo–accretionary wedge: The metamorphic rock record of prograde dehydration and transient high pore-fluid pressures along the subduction interface (Western Series, central Chile): Geosphere, v. 16, no. 3, p. 765–786, https://doi.org/10.1130/GES02227.1.

Science Editor: Shanaka de Silva
Guest Associate Editor: Gray E. Bebout

Received 23 December 2019
Revision received 13 February 2020
Accepted 23 March 2020

Published online 29 April 2020

Multiple veining in a paleo–accretionary wedge: The metamorphic rock record of prograde dehydration and transient high pore-fluid pressures along the subduction interface (Western Series, central Chile)

Jesús Muñoz-Montecinos[1,2,*], Samuel Angiboust[1,*], Aitor Cambeses[3,*], and Antonio García-Casco[2,4,*]

[1]Institut de Physique du Globe de Paris, Université de Paris, CNRS, F-75005 Paris, France
[2]Department of Mineralogy and Petrology, Faculty of Sciences, University of Granada, Campus Fuentenueva s/n, 18002 Granada, Spain
[3]Institut für Geologie, Mineralogie und Geophysik, Ruhr-Universität Bochum, Bochum 44801, Germany
[4]Instituto Andaluz de Ciencias de la Tierra, CSIC–Universidad de Granada, Armilla, Granada 18100, Spain

ABSTRACT

High pressure–low temperature metamorphic rocks from the late Paleozoic accretionary wedge exposed in central Chile (Pichilemu region) are characterized by a greenschist-blueschist lithological association with interbedded metasediments that reached peak burial conditions of ~400 °C and 0.8 GPa during late Carboniferous times. We herein combine new extensive field observations, structural measurements, and geochemical and petrological data on vein and matrix material from Pichilemu transitional greenschist-blueschist facies rocks. The studied veins were first filled by albite, followed by quartz and calcite as well as glaucophane and winchite. Field, structural, and microscopic zoning patterns show that these rocks underwent a protracted sequence of prograde vein-opening events, which have been largely transposed to the main foliation before and during underplating in the basal accretion site near 25–30 km depth. While some of the earliest albite-filled vein sets may have formed after prograde breakdown of sub–greenschist facies minerals (<250 °C), our thermodynamic modeling shows that relatively minor amounts of fluid are produced in the subducted pile by dehydration reactions between 250 and 400 °C along the estimated geothermal gradient. It also confirms that the formation of interlayered blueschist and greenschist layers in Pichilemu metavolcanics is a consequence of local bulk composition variations, and that greenschists are generally not formed due to selective exhumation-related retrogression of blueschists. The early vein sets are a consequence of prograde internal fluid production followed by sets of hydrofractures formed at near-peak burial that are interpreted as a record of external fluid influx. We postulate that such a fractured sequence represents a close analogue to the high-Vp/Vs regions documented by seismological studies within the base of the seismogenic zone in active subduction settings.

*E-mail: jesus.munozmontecinos@gmail.com; angiboust@ipgp.fr; aitor.cambeses@rub.de; agcasco@ugr.es

INTRODUCTION

Blueschist-facies metamorphic rocks exhumed from ancient subduction interfaces enable documentation and understanding of fluid-rock interaction occurring near the downdip end of the seismogenic zone (Bebout and Barton, 1993; Halama et al., 2014; Angiboust et al., 2015) where episodic tremor and slow-slip events nucleate (Obara, 2002; Audet et al., 2009; Peng and Gomberg, 2010). The most obvious marker of fluid transport in metamorphic rocks is vein systems (e.g., Fyfe et al., 1978; Fisher and Brantley, 1992). Their geometry sheds light on the connectivity of fluid pathways as well as on the spatial and temporal scale of the fluid-rock interaction events (Zack and John, 2007). Textures recorded in veins yield information on crack aperture as well as crystal growth kinetics during each veining event (Cox and Etheridge, 1983; Bons, 2001), while vein-filling mineral assemblages and fluid inclusions provide a valuable source of information on fluid chemistry and pressure-temperature regimes of fluid migration (e.g., Philippot and Selverstone, 1991; Scambelluri and Philippot, 2001; Raimbourg et al., 2018).

Previous work on metamorphic rocks has demonstrated that the vein-filling material can either be of local origin, resulting from diffusion processes between the host and an almost stagnant fluid produced by local dehydration reactions (e.g., Spandler and Hermann, 2006), or from external provenance, resulting from advective transport over kilometer-scale distances before deposition in the crack (Etheridge et al., 1984; Cartwright and Barnicoat, 1999; Bebout and Penniston-Dorland, 2016; Lewerentz et al., 2017; Jaeckel et al., 2018). Fluid-inclusion thermometry has been also used to propose that the fluid phase from which the vein-filling material precipitates was warmer than the host, thus advocating for fast advective flow (Vrolijk et al., 1988). While short-distance diffusive transport does not require large-scale connectivity, transportation over hundreds or thousands of meters implies the presence of highly permeable pathways such as brittle faults (e.g., Sibson, 2013; Angiboust et al., 2015; Dielforder et al., 2015). Yet, the genetic link between individual

veining events, connection of vein networks by larger fault systems, and the fate of fluids along the interface over several seismic cycles requires further investigation (e.g., Husen and Kissling, 2001; Fagereng et al., 2010). The relative timing of vein formation with respect to matrix deformation during burial and/or exhumation as well as the link with paleoseismic events also requires further documentation (e.g., Dielforder et al., 2015).

Another consequence of fluid-rock interaction at depth is the variable metasomatic imprint that obliterates the original geochemical signature of the affected lithologies (e.g., Harlow and Sorensen, 2005; Vitale Brovarone et al., 2014; Bebout and Penniston-Dorland, 2016). Selective retrogression due to exhumation-related fluid circulation may enhance, in specific cases, the formation of blueschists and greenschists interlayered at centimeter to meter scale (e.g., Bröcker, 1990; Barrientos and Selverstone, 1993; Halama and Konrad-Schmolke, 2015). However, many studies have proposed that bulk-rock geochemical differences may lead to the equilibration of cofacial greenschists and blueschists in the subducted material (Dungan et al., 1983; Owen, 1989; Baziotis and Mposkos, 2011; Hyppolito, 2014). It has been proposed that Fe_2O_3 and Na_2O abundances and Fe/Mg and Na/Ca ratios can control the occurrence of actinolitic and glaucophanitic amphiboles, allowing for the formation of blueschists and/or greenschists (e.g., Dungan et al., 1983; Owen, 1989). This example highlights the importance of accurately constraining the metamorphic conditions of fluid-rock interaction because the consequences of different conditions in terms of subduction-zone fluid budget are drastically different.

Here we study a fully exposed, exhumed transitional greenschist-blueschist facies segment of a late Paleozoic paleo–accretionary wedge from central Chile (Pichilemu region) that provides a great opportunity for linking fossil subduction-related markers of fluid mobility such as vein systems together with structures and deformation patterns. The first part of this work aims at determining the controlling factors that result in the occurrence of layered blueschists and greenschists in this region because no consensus exists regarding the origin of this layering, interpreted either as a retrogressive fluid imprint or as a consequence of centimeter-scale bulk-rock composition variations (Hyppolito, 2014; Halama and Konrad-Schmolke, 2015). Resolving this issue is critical for the second part of this study, namely the design of a prograde fluid-production model that aims at understanding the chronology of vein-formation events, which will ultimately refine our vision of fluid mobility in active subduction margins.

GEOLOGICAL SETTING

In the Chilean Coastal Range, metamorphic rocks formed at the active Paleozoic continental margin, representing deformational records of the Gondwanan tectonic cycle, are exposed (Hervé, 1988) (Fig. 1). This tectonic cycle (Late Devonian–late Permian) is characterized by the subduction of oceanic crust under the continental margin of the southwestern part of Gondwana and formation of accretionary complexes (Ramos, 1988; Willner et al., 2005; Hyppolito et al., 2014a, 2014b), which were intruded by north-south–trending syn- and post-accretion subduction-related batholiths (Hervé et al., 2013; Charrier et al., 2015). The remnants of this paleo–accretionary wedge are now preserved in the Eastern (low-pressure) and Western (high-pressure) Series that form an almost continuous metamorphic belt (Aguirre et al., 1972; Hervé, 1988) extending between 34°S–54°S for >2000 km (Hervé, 1988; Angiboust et al., 2018) and interpreted as the result of coupled frontal and basal accretion in the subduction system (Richter et al., 2007; Willner et al., 2008).

At the Infiernillo locality (Figs. 1A–1C), close to Pichilemu city (34°23′30″S, 72°1′30″W), a NE-NNE–oriented meta-volcanosedimentary sequence belonging to the Western Series is composed of a mixture of continent-derived metasedimentary rocks (Willner et al., 2005), metapyroclastic rocks, metalavas, and meta–pillow lavas (Hervé, 1988; Hyppolito et al., 2014a). The main tectonic structure is characterized by a subhorizontal to subvertical penetrative foliation S2 that transposes the previous burial-related S1 and D1 fabrics (see below). Importantly, almost all outcrops at the Infiernillo locality show abundant veins ranging in size from millimeter to centimeter wide that have not been studied in detail so far. Willner et al. (2005) suggested that albite (± sodic amphibole) veins probably reflect precipitation from metamorphic fluids under peak metamorphic conditions. The metavolcanic rocks in the Pichilemu region exhibit relict pillow and hyaloclastite structures (e.g., Hervé et al., 1984; Willner, 2005) and have oceanic island basalt (OIB), enriched mid-ocean-ridge basalt (MORB), and normal MORB geochemical signatures, suggesting scraped-off sections of the subducting upper oceanic crust (Hyppolito et al., 2014a). These metabasites form meter- to decimeter-sized layers of greenschists and blueschists that underwent peak pressure-temperature (*P-T*) conditions of 0.70–0.93 GPa at 380–420 °C and 0.95–1.07 GPa at 350–385 °C, respectively (Willner, 2005). Their contrasting *P-T* conditions led Willner (2005) to suggest that greenschists and blueschists may represent different sections of the zone of basal accretion in the range from 25 to 40 km depth. At the Infiernillo locality, Hyppolito (2014) and Hyppolito et al. (2014a) classified the greenschist and blueschist metavolcanics as mostly OIBs that underwent uniform peak conditions of 0.75–0.80 GPa at 380–420 °C, and emphasized that such conditions correspond to the greenschist-blueschist transition (Fig. 1D). In contrast, Halama and Konrad-Schmolke (2015) proposed that interlayered greenschist and blueschist pairs are the result of selective retrogression of blueschists in the greenschist facies during exhumation. Retrograde metamorphism was estimated by Willner (2005) and Hyppolito (2014) at conditions of 0.40–0.80 GPa at 300–380 °C and 0.65 GPa at 360 °C, respectively (Fig. 1D).

Hyppolito et al. (2014b) concluded that garnet mica schists and amphibolites from the Western Series (Punta Sirena locality) formed under a hot subduction scenario (geothermal gradient of up to 16 °C/km) at ca. 340 Ma ($^{40}Ar/^{39}Ar$ amphibole and phengite ages) representing the earliest stages of the subduction event. Phengite ages from mature subduction blueschists and metapsammopelitic rocks from the Western Series yielded ages ranging between 292 ± 1 Ma and 308 ± 1 Ma ($^{40}Ar/^{39}Ar$ plateau ages), interpreted as reflecting the peak of the high-pressure (HP) metamorphism and the formation of the transposition foliation (S2 in Willner

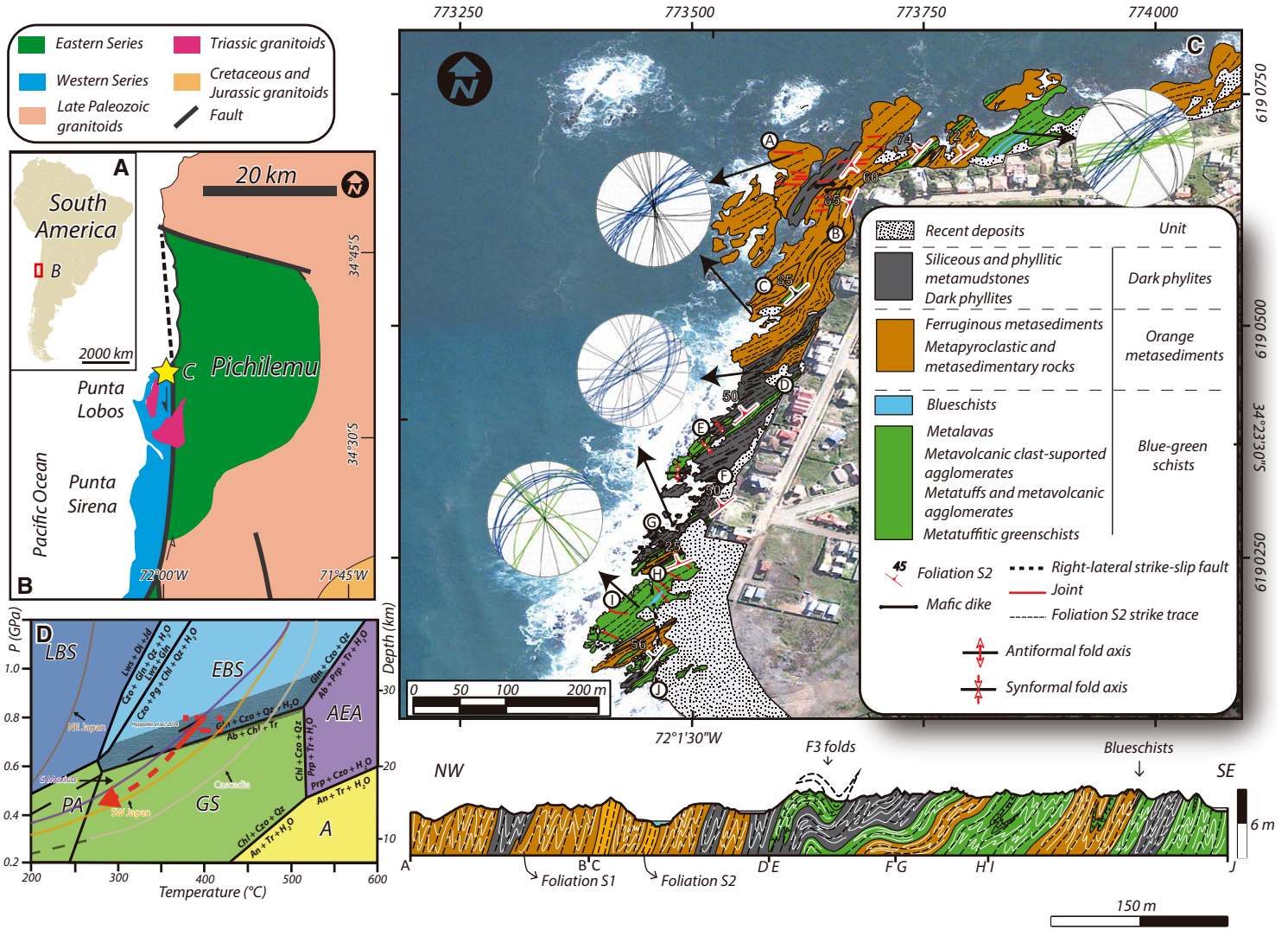

Figure 1. (A) Location of the studied zone relative to South America. (B) Simplified geological map of the Pichilemu region, Chile. (C) Detailed geological-structural map and cross-section profile of the studied zone at Infiernillo (modified from Hyppolito et al., 2014a). Blue, green, and black planes in the lower-hemisphere, equal-area stereoplots correspond to veins oriented parallel to the main foliation, transposed (oblique section), and cross-cutting veins, respectively. Circled letters correspond to the path followed in the cross section below. UTM and latitude and longitude coordinates are shown. (D) Pressure-temperature (*P-T*) diagram showing calculated peak and retrograde metamorphic conditions of the blue-green schists at the Infiernillo locality (red dashed box and arrow; after Hyppolito, 2014). Dashed black line corresponds to a subduction *P-T* path of 15 °C/km. *P-T* paths from Cascadia, Japan, and Mexico are shown (after Peacock et al., 2002). Background calculated fields from Evans (1990). PA—pumpellyite-actinolite facies; GS—greenschist facies; A—amphibolite facies; AEA—albite-epidote amphibolite facies; EBS—epidote-blueschist facies; LBS—lawsonite-blueschist facies. Mineral abbreviations from Whitney and Evans (2010): Ab—albite; Act—actinolite; Amp—amphibole; An—anorthite; Ap—apatite; Cal—calcite; Chl—chlorite; Chm—chamosite; Clc—clinochlore; Cpx—clinopyroxene; Czo—clinozoisite; Di—diopside; Ep—epidote; Fgl—ferroglaucophane; Fsp—feldspar; Gln—glaucophane; Hbl—hornblende; Ilm—ilmenite; Jd—jadeite; Lws—lawsonite; Ms—muscovite; Ol—olivine; Opx—orthopyroxene; Pg—paragonite; Ph—phengite; Pl—plagioclase; Prp—pyrope; Px—pyroxene; Py—pyrite; Qz—quartz; Rt—rutile; Stp—stilpnomelane; Tr—tremolite; Ttn—titanite; Wnc—winchite. Gray-shaded area corresponds to the overlap among stability fields of the different metamorphic facies from Evans (1990).

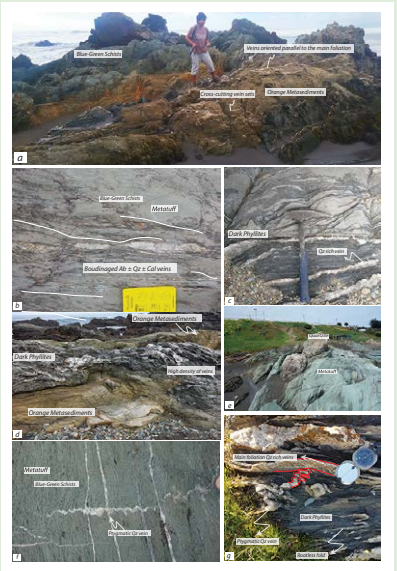

[1]Supplemental Materials. Figure S1: Additional field pictures and photomicrographs. Figure S2: Pseudosections of the blue-green schists, dark phyllites, and orange metasediments. Figure S3: Histograms of calculated vein abundance showing the mean values and the confidence interval for the blue-green schists, orange metasediments, and dark phyllites. Figure S4: Amphibole composition and classification diagrams (lined symbols correspond to amphibole with $Al^{VI} < Fe^{3+}$). Table S1: Major and trace whole-rock geochemical analysis. Table S2: Normalized average surface estimation compositions (blue-green schists) and whole rock compositions (orange metasediments and dark phyllites), used in Perple_X calculations. Table S3: Vein abundance estimations and statistics. Table S4: "Synthetic minerals" model proportions and thermodynamically calculated H_2O released during burial. Please visit https://doi.org/10.1130/GES02227.S1 or access the full-text article on www.gsapubs.org to view the Supplemental Materials.

et al., 2005). In addition, in situ $^{40}Ar/^{39}Ar$ ultraviolet laser ablation ages in microfolds yielded variable ages ranging between 329 and 259 Ma with differences in individual samples of 32–44 m.y. These values were considered as retrograde mineral growth and recrystallization events during exhumation-related pressure release and slight cooling (Willner et al., 2005). U-Pb zircon ages of ca. 305 Ma were obtained in subduction-related granitoids intruding the Eastern Series (Willner et al., 2005). The HP event of the Western Series and the main pulse of the magmatic activity and low-pressure metamorphism of the Eastern Series were therefore considered as coeval by Willner et al. (2005). The sequence has been lately intruded by granitoids that yielded U-Pb zircon and Rb-Sr mineral and whole-rock isochron ages between 257 and 220 Ma (Lucassen et al., 2004; Willner et al., 2005) and considered as the late magmatic activity associated with the retreat of the subducting slab.

FIELD OBSERVATIONS

General Structure

Petrological and structural observations at the Infiernillo locality lead to the identification of three coherent intercalated units: (1) blue-green schists, (2) dark phyllites, and (3) orange metasediments (Figs. 1C, 2A). The blue-green schists unit is characterized by abundant metatuffs, metalavas, and meta–pillow lavas metamorphosed under high pressure–low temperature (HP-LT) transitional greenschist-blueschist facies conditions (Figs. 1D, 2A–2D; Willner et al., 2005; Hyppolito et al., 2014a; Hyppolito, 2014). Blueschists and greenschists occur intercalated at centimeter to meter scale (Fig. 2C). Massive decameter-sized bodies of metabasalt are present in the Infiernillo locality and also further to the south (Punta Lobos locality). Blue rims in meta–pillow lavas and epidote-bearing veins in the inter-pillow space reflect spilitization during seafloor fluid-rock interaction (Fig. 2B). Evidence for a HP-LT metamorphism event is attested by the ubiquitous presence of Na-amphibole as cores, rims, and euhedral pristine crystals in the blueschist and greenschist host-rock and vein domains (Fig. 2D). Previous works have suggested that the peak metamorphic event occurred related to underplating and basal accretion processes, allowing the formation of a subhorizontal transposition main foliation S2 and intrafolial isoclinal folds, the latter corresponding to remnants of a (poorly preserved) prograde, S1 foliation (Glodny et al., 2005; Richter et al., 2007; Hyppolito, 2014). The main foliation structure is heterogeneously folded (F3), allowing a crenulation cleavage S3 that is much more developed in the dark phyllites, likely related to exhumation (Richter et al., 2007). Local S-C mylonitic fabrics suggest a non-coaxial kinematic regime.

The dark phyllites unit (Fig. 2E) corresponds to a strongly foliated sequence of phyllites with abundant carbonaceous (graphitic) matter and vein networks oriented mostly parallel to the main foliation (Fig. 2E). The orange metasediments unit is a metasedimentary sequence with abundant iron oxides and stilpnomelane, giving its characteristic orange-reddish color. The protoliths correspond to felsic pyroclastic rocks, conglomerates, breccias with volcanogenic fragments, quartzite, cherts, and sandstones, most of them representing terrigenous trench-filling sediments supplied from the overriding continental crust (e.g., Willner, 2005). As in the previous cases, the main structural fabric is a well-developed foliation S2 comprising abundant veins oriented parallel to the main foliation (Fig. S1A[1]). Interestingly, quartzite boudins stretched parallel to the main foliation are wrapped by metatuffs from the blue-green schists (Fig. S1E). Field markers of potential coseismic deformation such as pseudotachylytes and cataclasites (e.g., Fagereng and Toy, 2011; Angiboust et al., 2015) were not observed. Some albite veins exhibit brittle deformation overprinted by transitional greenschist-blueschist facies ductile shearing (Fig. 2F). In many cases, such prograde brittle features have been erased due to deformation during peak to retrograde metamorphism.

Structure and Distribution of Vein Networks

Three main vein sets were identified after structural characterization (stereonets shown in Fig. 1C). In the blue-green schists, the most abundant set corresponds to centimeter- to tens of centimeters–wide veins oriented parallel to the main foliation (blue planes in Fig. 1C), which contain albite + quartz + calcite ± amphibole (Fig. 2D). The distribution of these minerals is heterogenous, ranging from complex veins containing all of the aforementioned minerals to almost monomineralic veins. Additionally, veins of this type have been boudinaged (Fig. S1B [footnote 1]) as a consequence of shearing, likely during subduction (see below). No relationship was observed between vein density and the nature of the blueschist or greenschist host, as well as no retrogression is present in wall rock adjacent to veins. Millimeter- to tens of centimeters–wide quartz ± albite ± calcite veins occur in the dark phyllites and orange metasediments following the main foliation (e.g., Fig. 2E; Fig. S1A). These veins are heterogeneously distributed, showing striking differences in abundances at centimeter scale or in adjacent lithotypes (Figs. S1C and S1D). A second vein set is present in the blue-green schists and dark phyllites. Its mineral assemblage is similar to that of the first vein set. This vein set is distinguished from the first vein set by the fact that the planes of the veins clearly exhibit reorientation due to shearing (see green planes in Fig. 1C). They systematically exhibit segments of veins that obliquely cut across the main foliation (as shown on the stereographic projections in Fig. 1C). Here we refer to this category of veins as transposed veins (Fig. 2F; see Discussion). The third set of millimeter- to centimeter-wide quartz-rich veins occurs nearly perpendicular to the main foliation (see black planes in Fig. 1C). No clear cross-cutting relationship was observed between transposed and foliation-parallel veins. In addition, the third set of quartz-rich veins is folded with axial planes subparallel to the main foliation, forming ptygmatic veins and rootless folds as a consequence of flattening and shearing (Figs. S1F and S1G [footnote 1]). In the blue-green schists, high-density and chaotic calcite-rich vein networks are also present, ranging from millimeters to several centimeters in width (Fig. S1I). Host-rock fragments as much as tens of centimeters wide are bounded by these calcite-rich networks (Fig. S1I). Some of these veins are also

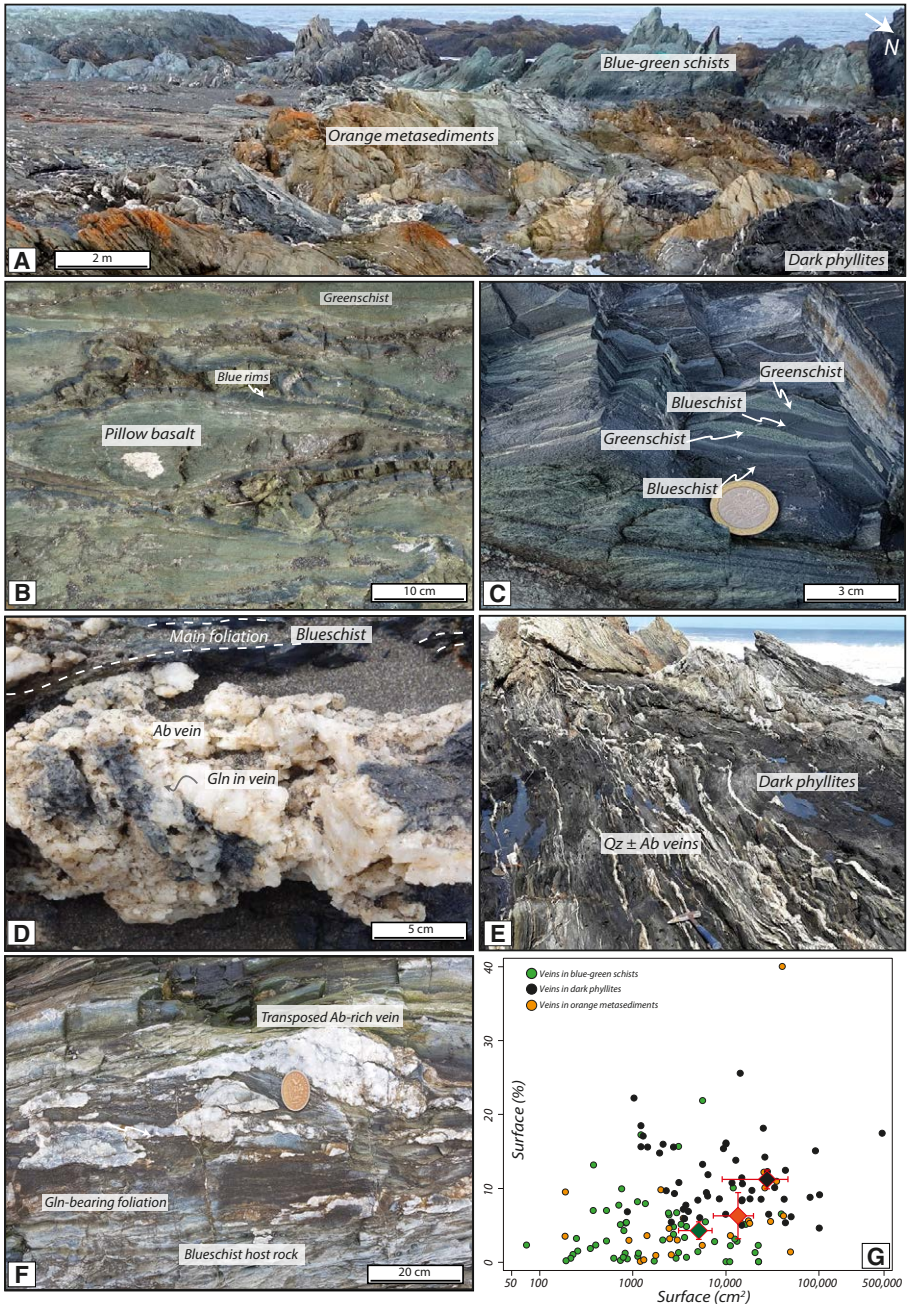

Figure 2. (A) General views of Infiernillo exposures; note the complex relationship between the blue-green schists, dark phyllites, and orange metasediments. (B) Pillow-lava structure in a metabasalt from the blue-green schists, in which the rim is richer in blue amphibole relative to the central green core. (C) Sharp contact relationship between centimeter- to millimeter-wide blueschist and greenschist layers in the blue-green schists. (D) Blue amphibole (glaucophane, Gln) in an albite (Ab) vein from the blue-green schists following the main foliation. (E) General view of the dark phyllites. Note the great abundance of quartz (Qz) ± albite veins following the main foliation. Standard geological hammer (45 cm long) as scale. (F) Sheared and transposed albite-rich veins in blueschist; note the sigmoidal shape of the albite veins and how they follow and at the same time transect the main foliation. The veins are fragmented at the tip of the sigmoid. (G) Surface measurements diagram showing the surface percentage of veins (surf%) relative to the surface area of the rock (in cm²), including the mean values (diamonds) and error bars (at a 95% of confidence interval) for each unit. For further calculations, the value of 0.9 surf% for the blue-green schists relative to the entire beach is considered here composed of 0.45 and 0.45 surf% of albite and quartz respectively, according to textural analysis.

folded with an axial plane subparallel to the main foliation, suggesting similar deformation conditions to those invoked for the ptygmatic veins. Quartz-rich necks and hydrofractures are observed perpendicular to the stretching direction of boudinaged orange metasediments (Fig. S1H). These vein sets were folded with axial planes subparallel to the boudin stretching direction and main foliation orientation (Fig. S1H).

METHODS

Vein Abundance Estimations

Total vein surface proportions (surf%) were estimated after processing 136 selected high-resolution field pictures supported with field measurements for each unit. An infinite projection in the dip direction is assumed, thus enabling direct conversion from surface percent to volume percent, considering the mean value to a 95% confidence interval. The absolute amount of veins (surf%) in the entire beach is calculated by multiplying the mean of the vein surface (surf%; Table S3) results by the respective proportion of each unit at the scale of the beach.

Analytical Methods

Petrological studies have been performed on representative vein and matrix samples from the blue-green schists, orange metasediments, and dark phyllites. Electron probe microanalyses were performed at Sorbonne Université (Paris, France) with a CAMECA SXFive instrument under common analytical conditions (15 kV, 20 nA, wavelength-dispersive spectroscopy mode) using a 5 µm beam diameter. Standards used for calibration are the following: orthoclase (Al, Si, K), fluorite (F), rutile (Ti), Cr_2O_3 (Cr), wollastonite (Ca), tugtupite (Cl), albite (Na), MgO (Mg), Fe_2O_3 (Fe), and rhodonite (Mn). Table 1 presents selected analyses of major phases. Elemental X-ray maps were obtained with the same instrument applying the ZAF correction and with a Zeiss Evo MA 10 scanning electron microscope (SEM) at the Institut de Physique du Globe de Paris (Paris, France) using internal calibration standards. The images were processed with DWImager (García-Casco, 2007) and Matlab (version 2012) software. Baricentric ternary composition diagrams Al_2O_3'-CaO'-FeO' (ACF) and Al_2O3'-MgO'-FeO' (AMF) were constructed by means of algebraic methods (Singular Value Decomposition) using software CSpace (Torres-Roldán et al., 2000), projecting from and along the appropriate phases and vectors to condense the 10- and 11-dimension compositional spaces, respectively. This type of diagram enables the identification of schematic phase relations and the compositional influence of the protoliths in the observed paragenesis as well as compositional trends expected after alteration (or other processes).

Amphibole nomenclature, structural formulae, and Fe^{3+} calculation are based on the recommendations of Leake et al. (1997). Here we refer to Na-amphibole as glaucophane, Na-Ca amphibole as winchite, and Ca-amphibole as actinolite because other amphibole species are rather scarce (see compositions in Fig. S4 [footnote 1]).The white mica structural formula was normalized to 11 equivalent oxygens assuming no Fe^{3+} in the octahedral site. Mineral compositions are given in atoms per formula unit (apfu). Mineral abbreviations are from Whitney and Evans (2010).

Representative samples from each unit (six from the blue-green schists, three from the orange metasediments, and three from the dark phyllites) were pulverized for major and trace element determinations performed by X-ray fluorescence (XRF) and inductively coupled plasma mass spectroscopy (ICP-MS) at Centro de Instrumentación Científica of the University of Granada (Granada, Spain). The first method (XRF) was conducted after fusion with lithium tetraborate with typical precision better than ±1.5% for an analyte concentration of 10 wt%, and the second (ICP-MS) after lithium metaborate and tetraborate fusion and nitric acid digestion of 0.2 g of the sample. It is likely that Zr determinations were underestimated due to instrumental limitations of the ICP-MS method. For practical reasons, FeO values were calculated from original Fe_2O_3. Some of the whole-rock data presented here (Table S1 [footnote 1]) have been acquired after scanning with SEM the surface of polished thin sections, local compositional estimates from areas measuring 3 × 1.5 mm^2 each after a counting time of 20 s for each sector. Mg-number [Mg/(Mg + Fe^{2+})] is abbreviated as Mg#.

Pseudosections: Model Design

Calculations performed with Perple_X software version 6.8.1 (Connolly, 2005) provide information on rock mineral composition and proportions, in

TABLE 1. ELECTRON PROBE MICROANALYSIS MINERAL COMPOSITION AND CATIONS PER FORMULA UNIT IN THE BLUE-GREEN SCHISTS UNIT

Mineral group	Sample	Zone	SiO_2 (wt%)	TiO_2 (wt%)	Al_2O_3 (wt%)	Cr_2O_3 (wt%)	FeO (wt%)	MnO (wt%)	MgO (wt%)	CaO (wt%)	Na_2O (wt%)	K_2O (wt%)	Total (wt%)	H_2O* (wt%)	Si (apfu)	Al_{tot} (apfu)	Fe^{3+} (apfu)	Fe^{2+} (apfu)	Mg (apfu)	Ca (apfu)	Na (apfu)	K (apfu)	# (O–OH)
Amphibole	P17A	Blueschist matrix	55.35	0.32	2.44	0.12	16.98	0.31	12.22	7.12	3.21	0.08	98.15	2.07	7.95	0.41	0.29	1.75	2.62	1.10	0.89	0.01	22-2
	P17A	Blueschist Ab vein	56.81	0.06	6.69	0.00	16.05	0.23	9.40	1.74	6.49	0.03	97.49	2.10	8.00	1.11	0.57	1.31	1.97	0.26	1.77	0.00	22-2
	P17A	Blueschist Ab vein	56.90	0.03	8.32	0.01	15.84	0.36	8.24	1.51	6.56	0.07	97.85	2.12	8.00	1.38	0.35	1.51	1.73	0.23	1.79	0.01	22-2
	P18.33	GS	57.61	0.10	6.75	0.04	15.66	0.20	9.89	1.92	6.49	0.04	98.70	2.13	8.00	1.10	0.54	1.28	2.05	0.29	1.75	0.00	22-2
	P18.33	BS	54.81	0.06	2.23	0.00	13.93	0.34	14.48	9.62	2.10	0.14	97.72	2.08	7.86	0.38	0.20	1.47	3.10	1.48	0.59	0.01	22-2
	P18.33	BS	56.98	0.02	1.23	0.00	12.69	0.39	15.64	10.44	1.42	0.06	98.88	2.12	8.04	0.20	0.00	1.50	3.29	1.58	0.39	0.01	22-2
	P18.33	BS	54.75	0.02	1.05	0.01	12.72	0.29	16.09	10.70	1.35	0.07	97.06	2.07	7.87	0.18	0.25	1.28	3.45	1.65	0.38	0.01	22-2
	P18.33	GS	55.57	0.09	5.64	0.02	16.46	0.14	10.05	2.20	6.27	0.05	96.48	2.07	7.96	0.95	0.55	1.42	2.15	0.34	1.74	0.00	22-2
	P18.33	GS	54.50	0.04	1.68	0.07	13.21	0.31	15.50	10.09	1.71	0.12	97.22	2.07	7.83	0.28	0.28	1.31	3.32	1.55	0.48	0.01	22-2
Chlorite	P18.33	GS	26.94	0.05	18.25	0.18	24.50	0.34	17.33	0.05	0.01	0.04	87.69	11.40	2.83	2.26	N.A.	2.15	2.72	0.01	0.00	0.01	10-8
	P18.33	BS	26.96	0.01	17.71	0.06	24.21	0.35	17.24	0.19	0.07	0.04	86.84	11.29	2.86	2.22	N.A.	2.15	2.73	0.02	0.01	0.01	10-8
Phengite	P18.33	BS	49.69	0.15	22.78	0.08	5.72	0.03	3.62	0.02	0.11	10.79	92.97	4.28	3.48	1.88	N.A.	0.33	0.38	0.00	0.01	0.96	20-4
	P18.33	BS	50.39	0.10	23.14	0.20	4.55	0.00	4.25	0.02	0.13	10.59	93.38	4.34	3.48	1.88	N.A.	0.26	0.44	0.00	0.02	0.93	20-4
	P18.33	GS	49.76	0.16	22.09	0.22	5.90	0.07	3.93	0.05	0.38	10.19	92.75	4.28	3.49	1.82	N.A.	0.35	0.41	0.00	0.05	0.91	20-4
	P18.33	BS	50.99	0.06	23.87	0.13	3.23	0.02	4.00	0.01	0.13	11.01	93.44	4.37	3.50	1.93	N.A.	0.19	0.41	0.00	0.02	0.96	20-4
	P18.33	GS	51.66	0.07	22.72	0.20	5.34	0.02	4.65	0.00	0.10	10.29	95.06	4.41	3.51	1.82	N.A.	0.30	0.47	0.00	0.01	0.89	20-4
	P18.33	GS	49.89	0.11	22.41	0.21	3.96	0.01	4.06	0.03	0.13	10.64	91.46	4.26	3.51	1.86	N.A.	0.23	0.43	0.00	0.02	0.96	20-4

Note: apfu—atoms per formula unit; tot—total; #(O–OH)—normalization defined in terms of O and OH relative to each mineral; BS—blueschist zone; GS—greenschist zone; Ab—albite; N.A.—not applicable.
*Calculated by stoichiometry.

addition to the assessment of phase relations at the *P-T* conditions of interest.

Pseudosections for the blue-green schists were calculated based on two chemical compositions (GS and BS zones; see Blue-Green Schists: Matrix section below) obtained using SEM surface estimations in the system Na_2O-CaO-K_2O-FeO-MgO-Al_2O_3-SiO_2-H_2O-TiO_2-O_2 (NCKFMASHTO), considering water-saturated conditions from 250 °C to 450 °C and from 0.50 to 1.00 GPa. Similar conditions were used for the dark phyllites and orange metasediments using averaged XRF whole-rock compositions (see Perple_X compositions in Table S2 [footnote 1]). For mineral solutions and aqueous fluid, the thermodynamic mineral database from Holland and Powell (1998; updated 2002) was used. The following solid-solution models were chosen according to the recommendations of Willner et al. (2016) for low-grade metamorphic conditions: Holland and Powell (2003) and Powell and Holland (1999) for white micas, epidote, chlorite, and biotite; Massonne and Willner (2008) for amphibole, pumpellyite, and stilpnomelane; and Holland and Powell (1996) for clinopyroxene. CO_2 is not considered in the pseudosection modeling approach because carbonates are almost absent in the host-rock matrix. The resulting pseudosections are presented as supplemental material (Fig. S2 [footnote 1]).

RESULTS

Vein Abundance Estimates

The results of the relative amount of vein abundance, by surface area, at the scale of the entire Infiernillo beach are shown in Figure 2G. Our estimates yield values of ~4.3 ± 1.2, ~6.3 ± 3.1, and ~11.2 ± 1.3 surf% for the blue-green schists, orange metasediments, and dark phyllites, respectively. Histograms showing the mean values and the confidence interval together with individual results are presented as supplemental material (Fig. S3; Table S3 [footnote 1]). The proportion of each unit at the scale of the entire Infiernillo locality (based on the high-resolution map from Hyppolito et al. [2014a]) are 21, 50, and 29 surf% for blue-green schists, orange metasediments, and dark phyllites, respectively. Thus, the resulting vein proportion in the full Infiernillo sequence yields a total value ~7.3 surf% of veins for the entire locality, with ~0.9, 3.1, and 3.3 surf% for the blue-green schists, orange metasediments, and dark phyllites, respectively (see Table 2).

Bulk-Rock Geochemistry and Petrology

In this section, geochemical analyses of the blue-green schists are presented in order to constrain the controlling factors resulting in the occurrence of interlayered blueschists and greenschists exposed at the Infiernillo locality. Petrographic and petrological analysis will also serve as a basis for a fluid-production model, which includes the three lithotypes of the studied sequence. Representative geochemical analyses of blue-green schist metavolcanics, avoiding outer rims of pillows, inter-pillows, and apparently spilitized meta–pillow lavas, together with compositions from previous studies are shown in Figures 3A–3H. We have plotted major elements against Mg#, because previous studies (e.g., Dungan et al., 1983; Palin and White, 2016) emphasized the important role of Mg in controlling the formation of blueschists and greenschists.

The Mg# is slightly higher in greenschists than in blueschists (Figs. 3A–3D). Al_2O_3 systematics (Fig. 3A) show extensive scatter with considerable overlap between blueschists and greenschists. CaO is higher in greenschists than in blueschists but with some overlap (Fig. 3B). Na_2O content is on average higher in blueschists than in greenschists (Fig. 3C) while the Na/Ca ratio (Fig. 3D) is commonly lower in greenschists than in blueschists.

TABLE 2. ESTIMATED SURFACE PROPORTIONS AT INFIERNILLO

Unit	Infiernillo absolute surface area (%)		
	Matrix	Albite veins	Quartz + calcite veins
Blue-green schists	20.10	0.45	0.45
Dark phyllites	25.74	0.00	3.26
Orange metasediments	46.86	0.00	3.14
Sum	92.70	0.45	6.85

Note: Albite veins are neglected in the dark phyllites and orange metasediments because they are scarce in these units.

The systematics described above are classically interpreted as the consequence of (1) magmatic differentiation and/or cryptic seafloor spilitization or (2) metasomatism during subduction or exhumation, as proposed by Halama and Konrad-Schmolke (2015). The abundance of immobile trace elements (Figs. 3E and 3F) shows that the studied blue-green schists are basaltic in composition and similar to OIBs (in line with Hyppolito et al. [2014a] and Halama and Konrad-Schmolke [2015]), ruling out magmatic differentiation as an important process affecting the suite of studied samples. In order to investigate the presence of metasomatism, trace elements and chemographic analysis using the ACF diagram were designed considering classical basaltic and alteration mineral assemblages (Figs. 3G, 3H, and 4A). As shown in the ACF projection (Fig. 4A), most of the non-spilitized and/or altered bulk compositions considered of the Infiernillo locality are compatible with a magmatic mineral assemblage composed of olivine (forsterite and fayalite) + clinopyroxene (augite) + orthopyroxene (enstatite and ferrosilite) + feldspar (plagioclase ± K-feldspar), similar to fresh OIB compositions. However, part of the fields defined by the studied rocks and OIBs overlap the field of seafloor alteration assemblages (epidote + chlorite ± muscovite), hampering any conclusion about (cryptic) seafloor metasomatism as an explanation for the geochemical variability of the studied suite of rocks, except for those samples that plot toward the high-Al side, as indicated in Figure 4A. In addition, trace element analysis using Ba/Rb versus K and K/Th versus Ba/Th ratios (Figs. 3G and 3H) show a clear correlation with compiled fresh OIB values instead of a seafloor metasomatic trend. Nevertheless, two samples clearly follow a HP metasomatic enrichment trend (see also Halama and Konrad-Schmolke, 2015).

In addition to the ACF diagram, we show the composition of the studied rocks in the AMF diagram (Fig. 4B) in order to analyze the effect of bulk-rock FeO and MgO variations in the context of schematic phase relations expected at HP (e.g., Palin and White, 2016). A clear trend can be distinguished,

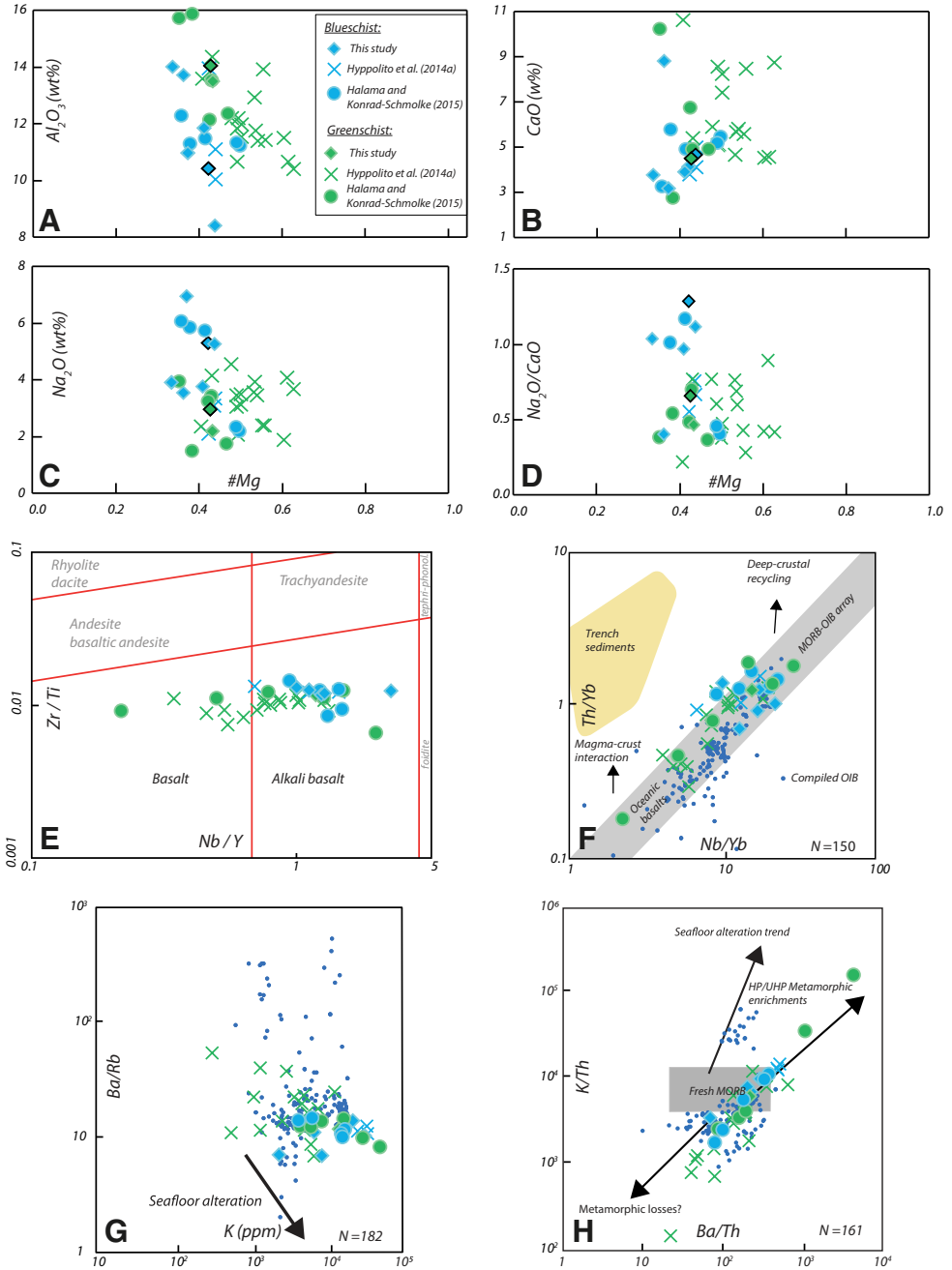

Figure 3. Geochemical analyses of the blue-green schists. (A–D) Major oxides Al_2O_3, CaO, Na_2O, and Na/Ca ratio versus Mg# [calculated as $Mg/(Mg + Fe^{2+})$]. Outlined symbols correspond to BS (blue) and GS (green) compositions, respectively. (E) Zr/Ti versus Nb/Y diagram (Winchester and Floyd, 1977; modified from Pearce, 1996). (Tephri-phonolite abbreviated as Tephri-phonol.) (F) Th/Yb versus Nb/Yb diagram (Pearce, 2008). Most of the samples plot in the oceanic basalts field, similar to compiled fresh oceanic island basalt (OIB). MORB—mid-ocean-ridge basalt. (G) Ba/Rb versus K diagram showing the seafloor alteration trend from Bebout (2007). (H) K/Th versus Ba/Th diagram showing seafloor alteration, high-pressure–ultrahigh-pressure (HP/UHP) metamorphic enrichments (metasomatic alteration according to Halama and Konrad-Schmolke [2015]) and metamorphic losses trends from Bebout (2007). OIB compositions from Galápagos and Hawaii are compiled from the GeoReM database (http://georem.mpch-mainz.gwdg.de/).

where (1) most of the blueschist samples plot within glaucophane-bearing assemblages and (2) most of the greenschist samples plot in the field of chlorite + actinolite–bearing assemblages compatible with classical greenschist facies parageneses. Some greenschists that plot within glaucophane-bearing assemblages may indeed be considered as retrogressed blueschists, in line with Halama and Konrad-Schmolke (2015). However, those authors have described the occurrence of glaucophane in all of their analyzed greenschist samples, in agreement with the plotting of these compositions within the glaucophane-bearing assemblages.

Textures and Microstructures

Dark Phyllites and Orange Metasediments: Matrix and Veins

Metasedimentary rocks from the dark phyllites and orange metasediments are essentially composed of phengite + quartz + organic matter + albite + chlorite ± titanite ± sulfides ± iron oxides, and phengite + quartz + albite + stilpnomelane ± chlorite ± titanite ± sulfides ± iron oxides, respectively. Phengite grains defining the main foliation as well as folded crystals forming a crenulation cleavage S3 are present. These crystals are in apparent textural equilibrium with quartz and albite, although some plagioclase detrital remnants

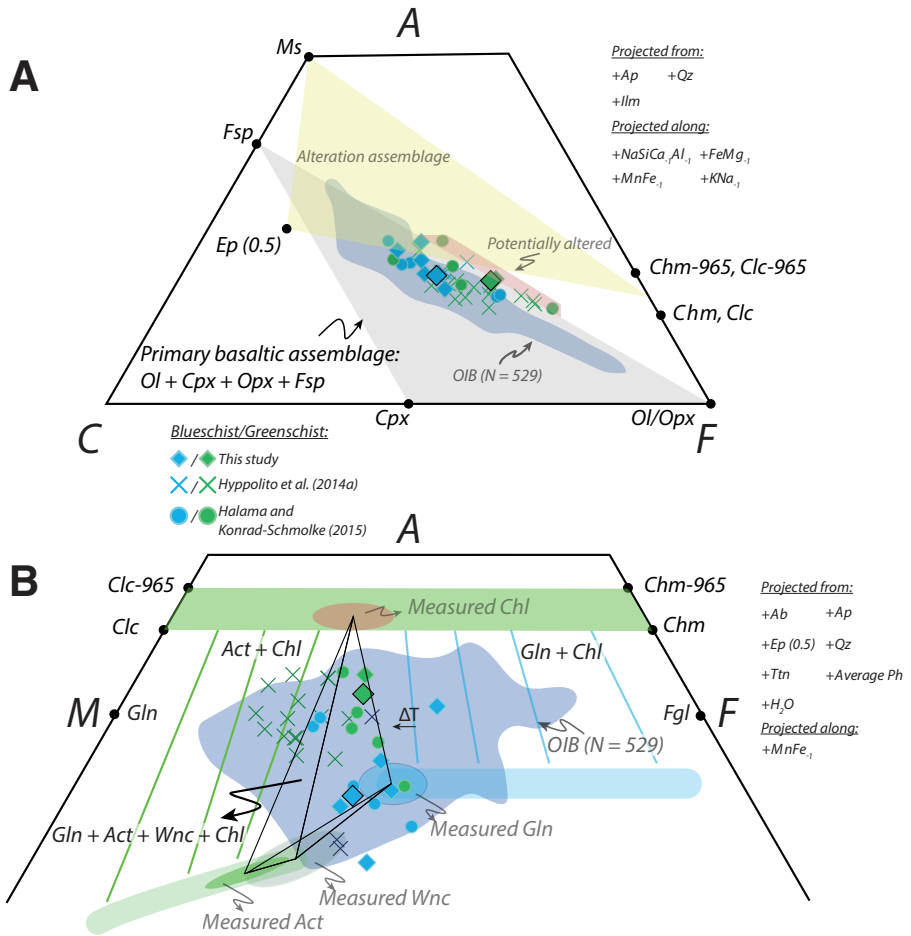

Figure 4. ACF and AMF (see Methods section for further details) triangular diagrams after projection of mineral chemical compositions and whole rock from (apatite, quartz and ilmenite and albite, apatite, epidote, titanite, quartz, phengite, and H_2O, respectively) phases and ($NaSiCa_{-1}Al_{-1}$, $FeMg_{-1}$, $MnFe_{-1}$ and KNa_{-1} and $MnFe_{-1}$, respectively) exchange vectors as indicated in each diagram. The diagrams have been truncated towards the A apex for aesthetic reasons. For mineral abbreviations, please refer to Figure 1 caption. (A) ACF (Al_2O_3'-CaO'-FeO') projection. The basaltic assemblage corresponds to a typical basalt containing plagioclase, olivine, and pyroxene. The alteration assemblage corresponds to ocean-floor metamorphism and/or metasomatism forming chlorite, epidote, and muscovite. (B) AMF (Al_2O_3'-MgO'-FeO') projection representing phase relationships of studied and reported blueschists and greenschists at the Infiernillo locality. The tie-triangle Gln + Act + Chl moves toward higher MgO (M) contents upon temperature increase (modified from Spear, 1993). Chm and Clc-965 refer to chamosite and clinochlore with Fe-Mg, Al, and Si of 9, 6, and 5 atoms per formula unit, respectively (Spear, 1993). Ep (0.5) refers to epidote with 50% of pistacite component. Oceanic island basalt (OIB) compositions are from Juan Fernández, Galápagos, and Hawaiian Islands compiled from the GeoReM database (http://georem.mpch-mainz.gwdg.de/). Outlined symbols correspond to the blueschist (BS) and greenschist (GS) zone compositions of the blue-green schist unit, calculated using energy-dispersive X-ray spectroscopy surface estimations.

occur. Stilpnomelane and chlorite, which both grow post-kinematically, are abundant in the foliation in the orange metasediments, together with iron oxides. Dark fringes of insoluble material are also present along the foliation, indicating that pressure-solution deformation mechanisms were active during deformation. Noteworthy is that carbonate phases are absent in the matrix of both units, even where they contain carbonate-bearing veins.

Representative vein textures can be seen in Figures 5A–5D. Veins in both the dark phyllites and orange metasediments are commonly subparallel to the main foliation and are composed mostly by blocky quartz and subordinate albite crystals that grow perpendicular to the host-rock contact (Figs. 5B and 5C). Minerals in these veins show undulose extinction, grain-boundary bulging, and recrystallization, mostly in quartz, suggesting dislocation creep as an important deformation mechanism. Collapse textures in the sense of Bons et al. (2012) were not observed. Inclusion tracks are abundant in quartz veins (Fig. 5B) and indicate several stages of reopening (e.g., Ramsay, 1980). Albite shows mostly brittle deformation with local kinking and incipient subgrain formation along grain boundaries (e.g., Fig. 5D). Quartz infiltrates previous albite veins (Fig. 5D) and also occurs as ribbons cross-cutting previous quartz grains. Calcite is seen (1) subordinately related to quartz in veins following the main foliation and (2) cross-cutting previous structures (Fig. 5B). Calcite also infiltrates along albite twins and occurs as late millimeter-sized veins together with chlorite and/or iron oxides.

Blue-Green Schists: Matrix

Blueschists and greenschists at the Infiernillo locality are medium- to fine-grained rocks slightly affected by retrogression. In general, blueschists correspond to strongly foliated fine-grained metatuffs with abundant glaucophane (locally riebeckite) + winchite (locally barroisite) + actinolite + albite + chlorite + phengite ± titanite ± apatite and scarce quartz, epidote, and sulfides. Few local relicts of pre-subduction hornblenditic amphibole are overgrown by actinolite mantles and glaucophane rims

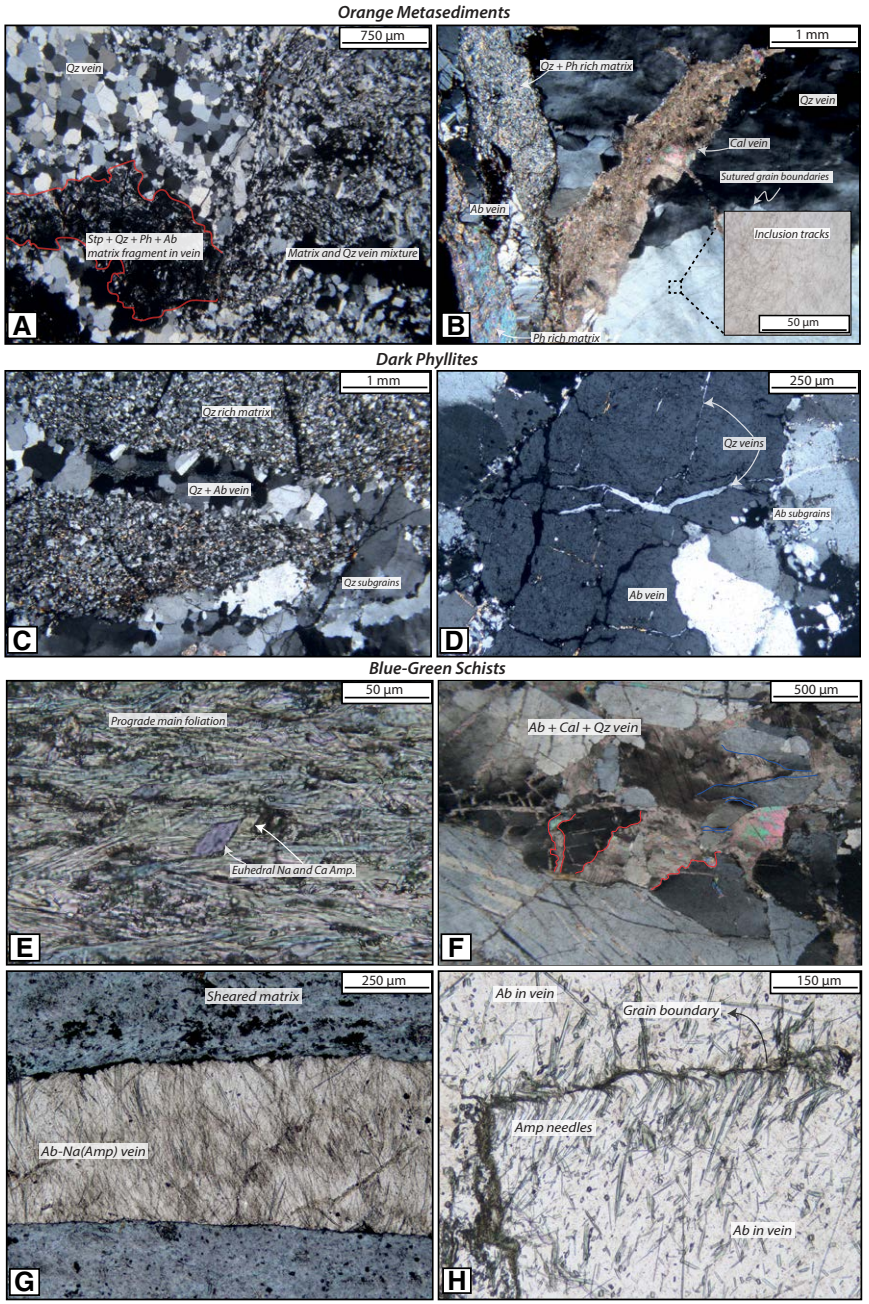

Figure 5. Optical photomicrographs of selected samples from the orange metasediments (A and B), dark phyllites (C and D), and blue-green schists (E–H). For mineral abbreviations, please refer to Figure 1 caption. (A) Cross-polarized view of a stilpnomelane + quartz + phengite + albite matrix fragment in a quartz vein. (B) Cross-polarized view of a coarse-grained quartz vein cut by calcite (center and right part); note the inset showing inclusion tracks in the quartz vein and the phengite + quartz matrix transected by an albite vein oriented perpendicular to the contact with the host rock (lower left part). (C) Cross-polarized view of a fine-grained matrix composed by quartz + phengite + albite being cut by a coarse-grained quartz vein with subordinated albite; note the subperpendicular orientation of albite crystals growing from the vein contact toward the center of the vein. (D) Cross-polarized view of an albite + quartz vein; note the irregular contacts and slight kinking of albite twins. (E) General view of a blue-green schist (sample P18.33); note the blue and green colors of euhedral amphibole crystals occurring in sharp contact overgrowing an earlier prograde amphibole main foliation. (F) Cross-polarized view of an albite + calcite + quartz vein; note the hydrofracture filled by calcite; red and blue contours represent grain boundaries likely representing a former albite crystal (one crystal for each color). (G) Detailed view of contact relationships between the sheared matrix and albite + blue amphibole vein; note the orientation of blue amphibole needles perpendicular to the host rock. The greater amount of amphibole along vein walls is likely related to a diffusion-limited process, given that the source of Mg and Fe needed to grow amphibole in the albite vein is the matrix. (H) Detailed view of albite grain contacts with blue-green amphibole growing perpendicular to it and sheared.

(Fig. 6A). Albite occurs in the matrix either overgrown by glaucophane (Fig. 6B) or lining the foliation in apparent equilibrium with phengite, glaucophane, and winchite. The most abundant Ti-bearing phase in the foliation is rutile. However, titanite occurs in the vicinity of former plagioclase relicts, as a consequence of local calcium activity gradients on rutile-titanite stability (Angiboust and Harlov, 2017). On the other hand, greenschists are mostly metatuffs, metalavas, and meta–pillow lavas, the latter being weakly foliated in comparison to other rocks. Their mineral assemblage is mainly composed of actinolite + winchite + chlorite + albite + glaucophane + epidote + titanite and scarce sulfides and relict grains of igneous plagioclase and pyroxene. It is worth noting that in both the blueschists and greenschists, carbonate minerals are almost absent. Phengite compositions are summarized in Figure 7.

To investigate phase relationships and set the basis for a fluid-production model, we have selected

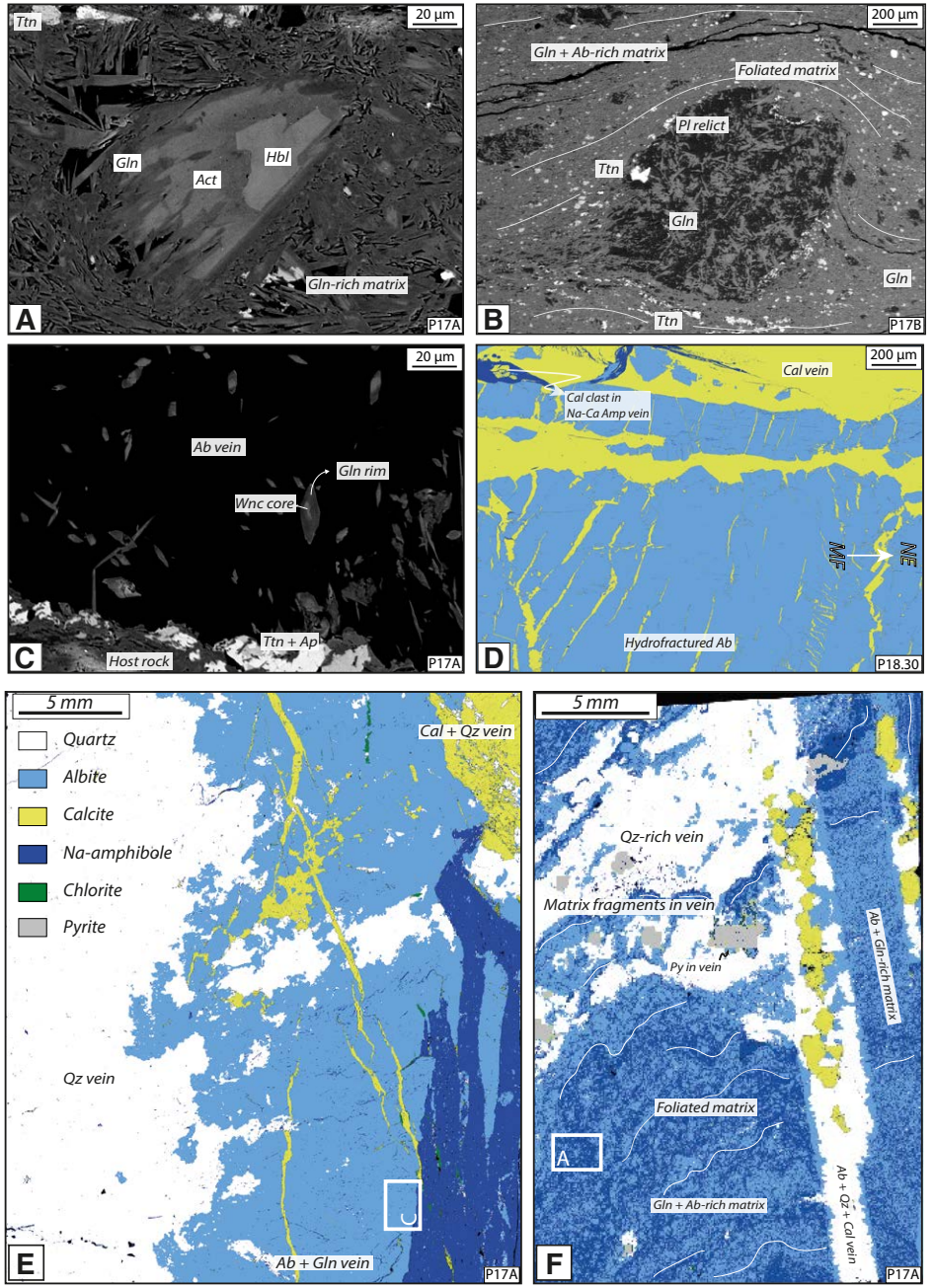

Figure 6. (A–C) Backscattered electron images of blue-green schists. For mineral abbreviations, please refer to Figure 1 caption. (A) Relict of hornblenditic amphibole replaced by actinolite and rimmed by glaucophane during prograde metamorphism close to high-pressure peak metamorphic conditions. (B) Plagioclase relict partially replaced by glaucophane in a fine-grained matrix; note the close spatial relationship between titanite and the plagioclase relict. (C) Albite vein with amphibole showing prograde zoning pattern (winchite core and glaucophane rim). (D–F) High-resolution energy-dispersive X-ray spectroscopy phase maps. (D) Albite vein with calcite veinlets showing hydrofracturing texture; note the calcite fragment in a Na- to Na-Ca-amphibole-rich vein. MF refers to the main foliation oriented to the northeast (NE). (E) Albite + quartz + calcite ± glaucophane vein; albite is oriented perpendicular to the vein wall; note the later quartz + calcite hydrofracture-like domain affecting the albite vein. (F) Quartz vein parallel to the main foliation as hydrofracture fabric affecting the foliated glaucophane + albite-rich matrix; note the host-rock fragments in the vein and the later blocky quartz + calcite + albite vein cross-cutting the previous quartz vein.

a blue-green schist sample (sample P18.33; Fig. 5E) that shows strong color contrasts at centimeter scale from blue to green, suggesting straightforward distinctive mineral assemblages and compositions across the sample. The blueschist zone (BS zone) is characterized by fine-grained glaucophane + winchite + titanite + albite ± actinolite ± phengite ± chlorite ± apatite ± iron oxides and sulfides, defining the penetrative main foliation (Figs. S1J and S1K [footnote 1]). Actinolite is in sharp contact with, as well as in thin overgrowing rims of, earlier glaucophane. The greenschist zone (GS zone) is characterized by higher abundances of chlorite and phengite compared to the BS zone. Glaucophane here is less abundant and occurs as cores and as prismatic euhedral crystals in the matrix, unlike winchite and actinolite, which are most abundant among amphiboles. Locally, glaucophane cores and actinolite rims are present.

Importantly, the absolute abundance of amphibole decreases toward the GS zone. A first generation of winchite grows parallel to the main foliation, followed by glaucophane and actinolite in sharp contact, overgrowing, in perfectly euhedral prismatic habit, earlier prograde winchite (Fig. 5E), reflecting a superimposed prograde metamorphic condition. Thus, the association between glaucophane and winchite is complex, growing in sharp contact or one rimming

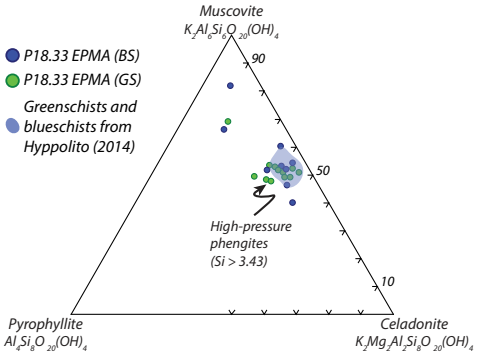

Figure 7. Triangular plot for phengite compositions in the blue-green schists. EPMA—electron probe microanalyses; BS—blueschist zone; GS—greenschist zone.

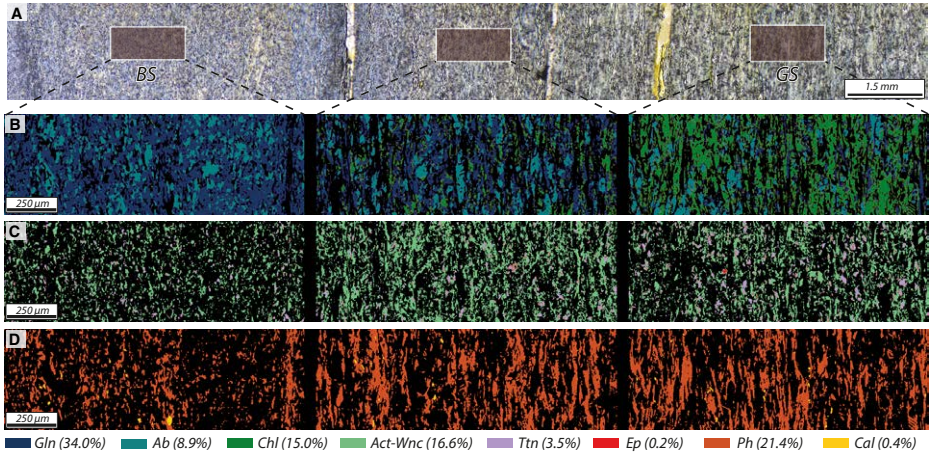

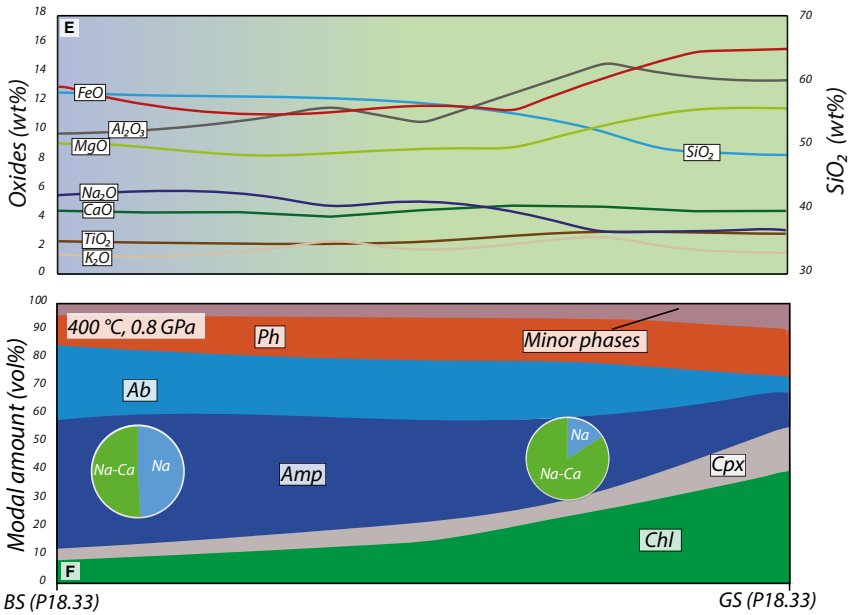

Figure 8. (A–D) Masks of three different zones from a single thin section of the blueschist-greenschist sample P18.33, based on X-ray maps. BS—blueschist zone; GS—greenschist zone. (A) Image showing the location and size of each X-ray map. (B–D) Phase distribution and abundance images of glaucophane + albite + chlorite, actinolite-winchite + epidote + titanite, and phengite + calcite, respectively (image created with DWImager software (García-Casco, 2007). (E) Compositional diagram showing variation in major oxides along an energy-dispersive X-ray spectroscopy surface estimation transect from the BS toward the GS zone. (F) Thermodynamically calculated phase abundance diagram at 400 °C and 0.80 GPa. Chemical composition variations (horizontal axis) were calculated for mixed BS-GS compositions. The pie charts show amphibole composition ratios; note that the calcic component in amphibole increases toward GS compositions. Minor phases include mostly quartz and titanite, among others. For mineral abbreviations, please refer to Figure 1 caption.

the other (e.g., glaucophane core with winchite rims and vice versa). Phengite in the BS and GS zones is rich in the celadonitic component (Fig. 7), with Si = 3.48–3.63 apfu, Mg# = 0.53–0.69, and very low Na (0.01–0.05 apfu). The minor differences in phengite composition between the BS and GS zones (Fig. 7) and the fact that no major retrogression-related textures occur suggest almost complete preservation of the transitional greenschist-blueschist facies metamorphism.

Phase abundances and compositional variations between centimeter-scale BS and GS zone intercalations can be clearly appreciated in high-resolution X-ray maps obtained in three zones from sample P18.33 (Figs. 2C and 8) as well as with the transect of SEM surface compositional estimates (Fig. 8E). As mentioned above, the selected sample P18.33 shows a clear difference in color from blue to green (Fig. 8A) reflecting variations in mineral abundances (Figs. 8B–8D). The left section (BS) clearly shows higher proportions of glaucophane and albite (Fig. 8B). Toward the GS zone, slightly less albite and markedly more chlorite, actinolite-winchite + titanite, and phengite proportions are observed (Figs. 8B–8D, respectively), together with a larger grain size and an increase in the calcic component in amphibole. Note that the relative amount of amphibole in the GS zone is lower compared to the BS zone. Toward the GS zone,

the foliation style changes from a very continuous and homogeneous pattern to an anastomosing-like fabric, probably due to a greater abundance of phyllosilicates (Figs. S1I–S1M [footnote 1]).

The changes observed in the estimated surface composition transect (Fig. 8E) are characterized by a SiO_2 and Na_2O decrease (by ~10.6 and ~2.3 wt% respectively) and an FeO, MgO, TiO, and Al_2O_3 increase (by ~2.9, 2.7, 2.8, and ~4 wt% respectively), reflecting the modal increase of chlorite, phengite, titanite, and actinolite from the BS toward the GS section. CaO and K_2O content show almost no variation. On the other hand, none of the studied vein margins exhibit selvages that could have witnessed local elemental mobility (e.g., see the sharp matrix margin on Fig. 6F).

To address the effect of bulk chemical composition variations at peak conditions (0.80 GPa and 400 °C; see Hyppolito, 2014), we developed a thermodynamic model for mixed BS-GS compositions (Fig. 8F). The calculation shows that major phase changes between the BS and GS zones are characterized by the increase of phengite and chlorite abundances, and an important decrease in the absolute amount of amphibole and albite. The relative amount of the calcic component in amphibole strongly increases (see pie charts Fig. 8F), in agreement with petrological analyses. Thermodynamic modeling, in line with petrographic observations (Figs. S1J–S1M [footnote 1]) and petrological analysis, thus confirms the importance of bulk-rock differences on the paragenesis.

Blue-Green Schists: Veins

In this section, we describe the petrology of the previously defined vein types (see Structure and Distribution of Vein Networks section above). Veins parallel to the main foliation and transposed (first and second sets) are composed of coarse-grained albite + quartz + fine-grained glaucophane and/or winchite (Figs. 5G, 5H, 6C, and 6E) and subordinate titanite, apatite, and iron sulfides. Albite crystals grew mostly perpendicular to the vein walls and show evidence of bending, subgrain formation, and recrystallization. Albite veins elongated parallel to the S2 fabric are also present (Fig. 6D). These veins exhibit inclusion tracks subperpendicular to the elongation orientation and are sharply crosscut by later calcite veins, with evidence for hydrofracturing. In addition, abundant coarse-grained quartz + calcite ± fine-grained winchite and actinolite (Figs. 5F, 6C, 6E, and 6F) occur oriented according to the previous albite veins with evidence of hydrofracturing also affecting the host rock (e.g., Figs. 5G, 6D–6F; Fig. S1I [footnote 1]). The third vein set, with no clear cross-cutting relationship with respect to the previously mentioned veins, is filled by quartz + calcite, and albite of minor importance in terms of size and abundance (e.g., Fig. 6F). Note that calcite vein fragments in winchite-rich veins are present (Fig. 6D). Finally, a late chlorite ± calcite vein set occurs cutting all previous vein sets (Fig. 6E), showing almost no evidence of deformation.

Amphibole in albite veins shows compositions similar to that in the matrix, with winchite cores and (volumetrically minor) glaucophane rims and vice versa (Fig. 6C). Hydrofracture fabrics can be seen in former albite veins and host rock (e.g., Figs. 5F, 6D–6F; Fig. S1I [footnote 1]). Like in metasediments, solid- and fluid-inclusion tracks are abundant in quartz. Calcite crystals show strong mechanical twinning. Quartz presents undulose extinction, subgrains, and strong recrystallization, evidencing recovery and crystal-plastic deformation processes. The homogeneous orientation of amphibole needles in vein sets is commonly subperpendicular to the walls of the host rock (Figs. 5G and 5H). Albite grain boundaries in veins are rimmed with winchite needles that grew perpendicular to the crystal margin (Fig. 5H). A summary of mineral occurrences in blue-green schist veins and matrix is presented in Figure 9.

Dehydration Models for Infiernillo Rocks

In order to estimate the fluid released by the metamorphic sequence of Infiernillo during burial, we developed a two-step dehydration model. The first step considers the fluid production at the very early stage of burial based on commonly reported mineral assemblages in the range from 0 °C and 0.01 GPa to 250 °C and 0.50 GPa. This approach has

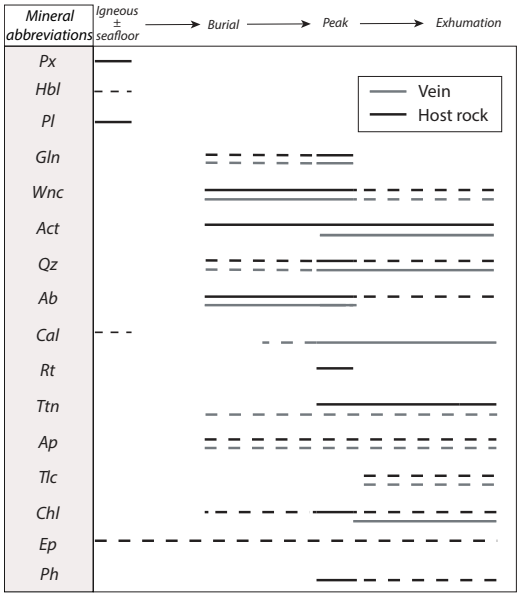

Figure 9. Diagram summarizing the mineralogical evolution of the blue-green schist matrix and veins. Dashed line indicates uncertainty in the mineral formation stage. For mineral abbreviations, please refer to Figure 1 caption.

been chosen because the pseudosection modeling technique is not well suited for very low-grade conditions (e.g., <250 °C). The second step corresponds to the thermodynamically calculated H_2O (in weight percent) released in the range of 250 °C and 0.50 GPa to 400 °C and 0.80 GPa using the Perple_X software. The sum of the fluid budget calculated for this two-step dehydration model corresponds to the total amount of H_2O released up to peak conditions.

"Synthetic Minerals" Modeling from 0 to 250 °C

To construct dehydration curves for the range from 0 to 250 °C (Fig. 10A), we assume theoretical mineral and abundances present along the prograde path (Table S4 [footnote 1]). From this approach, H_2O contents in minerals are considered together with H_2O contained in the porosity of the studied compositions. For further details on the calculation procedure, see Appendix 1 (see also a similar approach in Peacock [1993]). For the BS and GS compositions of the blue-green schists, an average of 25% of porosity (e.g., Whitmarsh, 1978; Carlson and Herrick, 1990) is assumed to be filled by pure H_2O (Fig. 10A). This porosity value dramatically decreases to values close to 0% in the first 3 km of burial (e.g., Whitmarsh, 1978; Carlson and Herrick, 1990). Here, a linear reduction of porosity is assumed, and the final value was set to 1%, in the same order of magnitude as calculated by Peacock et al. (2011) (see also Hyndman, 1988) for an overpressurized subducting slab. For the dark phyllites and orange metasediments, porosity values selected were 28% and 38% respectively (extrapolated from Magara, 1980), and a value of 1% was also assumed to be maintained up to peak conditions (Fig. 10A).

The main trends for the BS and GS compositions consist of a decrease in relict Ca-amphibole (hornblenditic), clinopyroxene, zeolite, and clay minerals and an increase in actinolite, clinochlore, and albite (Table S4 [footnote 1]). The H_2O contents for the two compositions dramatically decrease at the very early stage (Fig. 10A) due to porosity collapse followed by the consumption of clay minerals, zeolites, and stilpnomelane, releasing an average of ~8.0 wt% H_2O during burial.

For the dark phyllites and orange metasediments, the major changes consist of a decrease in smectite abundance and formation of illite, while quartz content is almost constant. H_2O contents for the two compositions dramatically decrease at the very early stage (Fig. 10A) due to porosity collapse followed by the nearly complete consumption of clays, releasing ~11.9 and 14.2 wt% of H_2O respectively.

Note that for every step of this calculation, we made sure that the synthetic assemblage had a bulk composition sufficiently close to the actual rock composition (i.e., difference of <8 wt% for SiO_2, <6 wt% for Al_2O_3, <3 wt% for FeO, <2 wt% for MgO, and <2 wt% for Na_2O and K_2O), assuming no or only very minor mass transfer of major elements during the prograde burial metamorphism (apart from H_2O).

Thermodynamically Calculated Models from 250 to 400 °C

Thermodynamic modeling for the BS and GS compositions in the range from 250 °C and 0.50 GPa to 400 °C and 0.80 GPa predicts a relatively similar trend of dewatering between them (Fig. 10B) with a different mineralogical evolution. Dehydration in the blue-green schist compositions is characterized by the consumption of stilpnomelane (Figs. 10C and 10D) and to a lesser extent lawsonite and chlorite (Fig. 10D).

Thermodynamic modeling for the dark phyllites and orange metasediments shows almost no dehydration in the considered *P-T* window (Figs. 10B, 10E, and 10F). In the case of the orange metasediments, stilpnomelane is fully consumed at the beginning of the path (Fig. 10F), followed by little to no prograde paragenetic evolution with increasing depth.

Considering both the "synthetic minerals" and the thermodynamically calculated models, the total H_2O released during burial up to peak conditions for the BS and GS compositions is 10.5 and 8.3 wt%, respectively, yielding an average of ~9.4 wt% of fluid. The total fluid released from the dark phyllites and orange metasediments during burial is ~12.0 and 14.4 wt%, respectively.

It is difficult to quantify the uncertainties associated with the low-temperature (0–250 °C) part of the model, because it is impossible to precisely ascertain the proportions of the considered minerals during the early stages of the subduction path and the porosity of the initial material. Because the amount of interstitial pore fluid was certainly high as expected for tuffaceous and sedimentary protoliths, we consider the high porosity values considered in our calculations (25–38 vol%) as realistic upper bounds (e.g., Magara, 1980; Carlson and Herrick, 1990). In addition, thermodynamic modeling results should also be taken with care due to (1) the strong heterogeneity of the sedimentary material forming the units and (2) the relatively high uncertainty of solid-solution thermodynamic properties at low-temperature conditions. Last, it should be also mentioned that a slight disagreement exists in the prograde evolution of metavolcanic units, because a minor amount of clinopyroxene (Fig. 8F) is thermodynamically predicted but not observed in the studied natural samples.

DISCUSSION

Petrological and microstructural investigations have revealed that evidence for HP metamorphism (including high-Si phengite and sodic amphibole) is ubiquitously found in all of the units forming the Infiernillo sequence. The tectonic history and microstructural imprint left by the burial-exhumation trajectory in Infiernillo rocks is also identical in all of the lithologies encountered in the coastal exposure. Altogether, these observations suggest that (1) the entire package now visible on the shore experienced HP-LT metamorphic conditions and (2) most of the imbrication of the different lithotypes occurred during burial-related shearing, before peak metamorphism. It is therefore straightforward that Infiernillo exposures represent a key natural laboratory to study fluid production, fluid-rock interaction, and subduction-related deformation

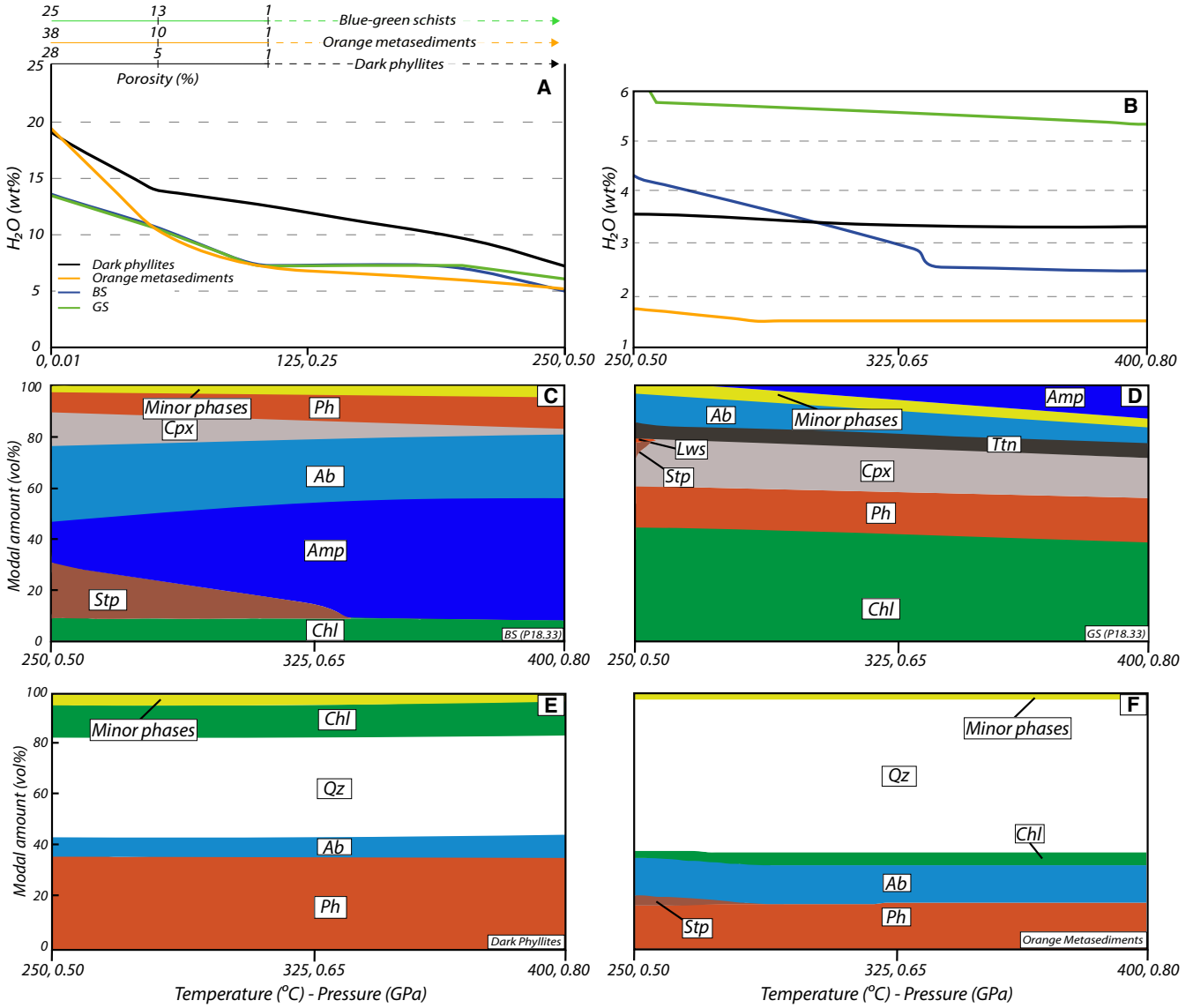

Figure 10. "Synthetic mineral" models and thermodynamically calculated H_2O contents and phase abundance diagrams. For mineral abbreviations, please refer to Figure 1 caption. (A) "Synthetic mineral" calculated H_2O content curves from 0 °C and 0.01 GPa to 250 °C and 0.50 GPa, showing fluid released during burial of the selected blue-green schist, dark phyllite, and orange metasediment compositions. Top arrows represent the variation in porosity values considered for each composition. Considered synthetic minerals are taken from natural mineral assemblages reported by Thompson and Humphris (1977) and Cho et al. (1986) for the blue-green schists, and Worden and Morad (2003) for the dark phyllites and orange metasediments. Densities are assumed to be constant through the path: 1 g/cm³, 2.9 g/cm³, and 2.4 g/cm³ for water, oceanic basalt, and shale and sandstone, respectively. BS—blueschist zone; GS—greenschist zone. (B) Thermodynamically calculated H_2O-fluid content curves from 250 °C and 0.50 GPa to 400 °C and 0.80 GPa, showing the fluid released from the selected blue-green schist, dark phyllite, and orange metasediment compositions. (C–F) Thermodynamically calculated phase amounts for BS (blue-green schists), GS (blue-green schists), dark phyllites, and orange metasediments, respectively. In all diagrams, the *x*-axis corresponds to temperature (°C), pressure (GPa).

within and at the downdip end of the seismogenic zone at maximum depths in the range of 25–30 km.

Blueschist and Greenschist Controlling Factors

In a previous study, Halama and Konrad-Schmolke (2015) proposed that the layering of Infiernillo metavolcanics is commonly related to layer-parallel fluid transport that caused selective retrogression resulting in the blueschist and greenschist intercalations seen in the field (Fig. 2C). In their model, the retrograde greenschist facies overprint would have stabilized winchitic and actinolitic amphibole at 0.40 ± 0.10 GPa, after generalized peak glaucophane-bearing assemblages. The amphibole zoning pattern observed here in the blue-green schist matrices and the apparent textural equilibrium between glaucophane and actinolite (e.g., Fig. 5E) confirm that most of the greenschist facies domains are not the result of a retrogressive metamorphism. In addition, phengite compositions show little variation (Fig. 7), also pointing to a very limited greenschist overprint, in agreement with Willner (2005). The ACF projection (Fig. 4A) shows that the elemental variations in most of the greenschists and blueschists at the Infiernillo locality can well be explained by primary magmatic paragenesis. Mobile and immobile major and trace element analyses (Figs. 3G–3H) support this statement, suggesting that seafloor metasomatism played a minor role and that fresh OIB compositions correlate well with those of the Infiernillo blue-green schists. However, seafloor fluid circulation evidently affected, at least locally, the rock volume as evidenced by the formation of rims around meta–pillow lavas (Fig. 2B). X-ray maps and SEM surface estimates (Fig. 8) show a clear trend of bulk-rock composition from the BS to the GS zone, resulting in variable amounts of glaucophane, actinolite, chlorite, and phengite. The AMF projection analysis (Fig. 4B) shows that geochemical differences between BS and GS compositions (Figs. 3A–3D) enhance the formation of glaucophane-bearing and actinolite-bearing rocks, respectively. The slightly higher Al proportions in the GS zone makes this composition favorable to form chlorite instead of glaucophane, while lower Al abundances in the BS composition enhance glaucophane formation making this composition to plot closer to the glaucophane apex, in agreement with petrological observations. It is important to note that OIB compositions fall in the actinolite + chlorite (± winchite) and glaucophane + chlorite (± winchite ± actinolite) fields, supporting the formation of both blueschist and greenschist parageneses at the same *P-T* conditions. Thereby, most samples indicate that major-element bulk composition correlates with the observed mineral paragenesis. Because the Mg# is the major factor controlling bulk-rock heterogeneities, we conclude that Infiernillo greenschists and blueschists are both stable at the same peak *P-T* conditions, and that important differences in the bulk-rock Mg# as well as local Al, Ca, and Na variations led to different paragenesis resulting in the millimeter-scale intercalation seen in the field in the transitional greenschist-blueschist facies (e.g., Fig. 2C).

This conclusion is partially in agreement with Dungan et al. (1983), who proposed that the Fe/Mg ratio together with the absolute amount of FeO_{total} determine the occurrence of blueschists and greenschists, the latter parameter being higher in blueschists. Here we observe that the absolute amount of FeO_{total} in our blueschists compositions is actually lower compared to the greenschists. Thus, we propose that the Fe/Mg ratio is a more important controlling factor than the absolute amount of FeO_{total}. These observations are in line with thermodynamic modeling results demonstrating that the observed phase assemblages of the BS and GS zones can be reproduced at fixed *P-T* conditions (Fig. 8F). We therefore conclude that the controlling factors resulting in blueschist and greenschist layers in the Infiernillo exposure, i.e., different amphibole compositions at peak conditions and the variable amount of phases, can be mainly explained by geochemical variability previous to the HP stage due to: (1) primary differences in the protolith composition likely related with igneous heterogeneities, and, to a lesser extent, (2) hydrothermal effects of seafloor fluids. However, some greenschists that plot in the glaucophane + actinolite + winchite + chlorite field (Fig. 4B) may represent retrogressed blueschists in agreement with samples that clearly show the HP metasomatic metamorphic enrichments trends illustrated in Figure 3H (as suggested by Halama and Konrad-Schmolke [2015]; see also Hyppolito [2014]).

Prograde Veining and Fluid-Production Model

Formation and Deformation of Veins

Natural observations in metamorphosed altered oceanic volcanic rocks have identified, among other reactions, analcime dehydration as an important fluid-producing reaction (e.g., Coombs, 1960):

$$\text{analcime } (NaAlSi_2O_6 \cdot H_2O) + \text{quartz} = \text{albite } (NaAlSi_3O_8) + H_2O. \quad (1)$$

According to this reaction, prograde analcime breakdown may enable the formation of the widespread albite veins identified in this study. In addition, the breakdown of calcic zeolites (e.g., laumontite, wairakite, heulandite) may also contribute large amounts of fluids. The observation of prograde zoning in albite vein amphibole suggests that these veins formed early during the burial history (i.e., before the blueschist facies overprint). We postulate that the texturally early albite veins visible in Infiernillo metavolcanics formed during zeolite facies mineral breakdown at temperatures <200 °C (Fig. 11A; according to the experimental data from Liou [1971]; see also Fyfe et al. [1978] and Spear [1993]). In other words, internally derived Na-rich fluids can easily explain the texturally earliest albite veins extensively observed in Infiernillo blue-green schists (Fig. 11). Some other vein sets, mainly filled by quartz, also may have formed as a result of burial-related mineral dehydration and compaction (Fig. 11A, inset 1). Synchronously, shear stresses favored orientation and reorientation (transposition) parallel to the developing main foliation (Fig. 11A, insets 1 and 2). In addition, quartz + calcite veins also show winchite and actinolite. Besides, the presence of calcite fragments in winchite-bearing veins help us to constrain their

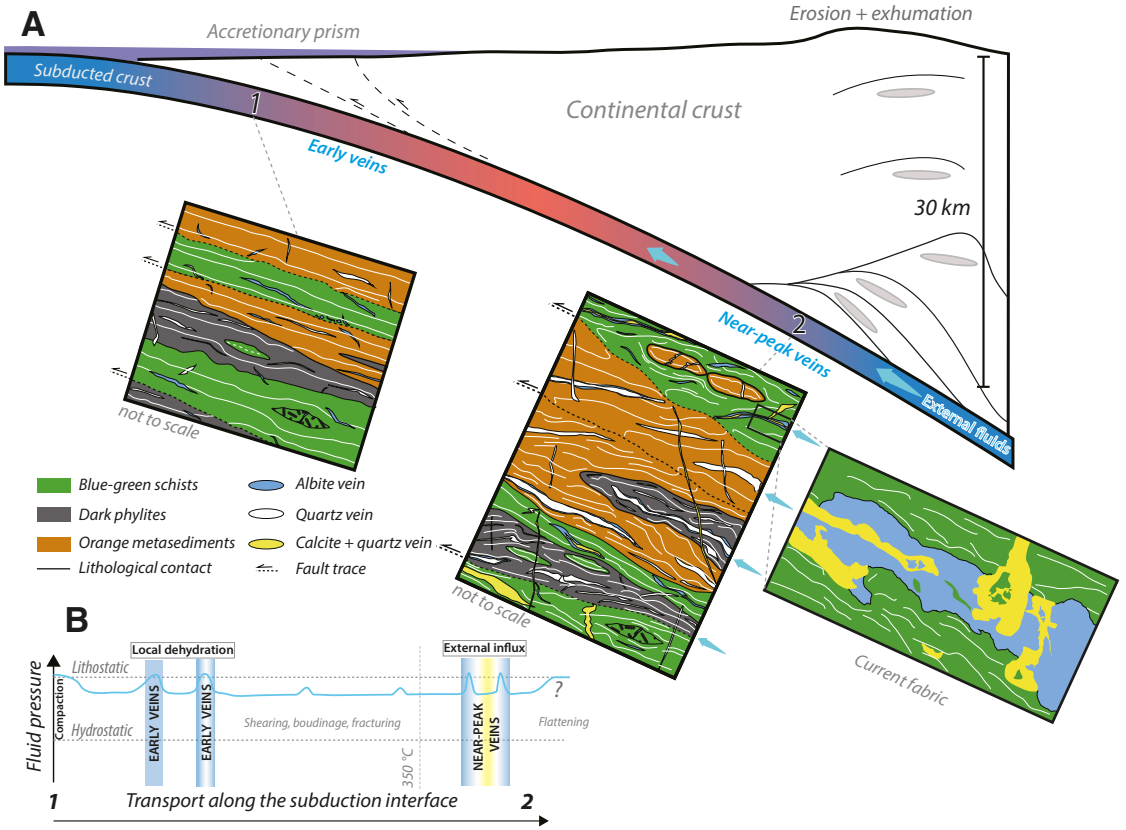

Figure 11. (A) Subduction zone sketch illustrating vein formation and evolution of Infiernillo rocks. (1) During early stages of subduction, the entire sequence underwent compaction and porosity collapse causing a massive release of fluids, cracking, and vein filling (with random orientations) together with hydrofracture-like fabrics commonly subparallel to the main rock structure (see also Moore et al., 1995). (2) Further down during prograde burial (at seismogenic-zone depths, in red), large amounts of fluids moving as pulses enhanced hydrofracturing (represented by the blue arrow), mainly through previous veins but also affecting the host rock and precipitating mostly quartz and calcite (as shown by albite and host-rock fragments in veins). Additionally, boudinaged orange metasediments were wrapped in matrix of blue-green schists developed close to peak conditions. Grey ovals are plotted in order to track the exhumation path. Duplex exhumation scheme is modified from Willner (2005). (B) Diagram showing fluid-pressure distribution (blue line) and deformation processes along the burial path (1 to 2) inspired by Saffer and Tobin (2011). Blue, white, and yellow shading in vertical bars refers to albite, quartz, and calcite+quartz vein precipitation events; see color code in A.

occurrence during burial, likely near peak conditions prior to exhumation (Fig. 6D). Approaching the HP stage, a supra-lithostatic pore-fluid pressure environment enabled fracturing followed by the precipitation of quartz + calcite ± albite as shown by (1) the hydrofracturing of the former albite veins (e.g., Figs. 5D–5F, 6D–6F; Fig. 11A, inset 2) and (2) the cross-cutting of the host rock by newly formed vein sets (Fig. S1I [footnote 1]). Once the imbricated slices of the subducted material were basally accreted and incorporated in the deep duplex (e.g., Richter et al., 2007), the veined sequence of Infiernillo became isolated from the fluid-rich subduction interface region, thus preventing new inputs from the plate interface region.

Elongated amphibole needles occur perpendicular to grain boundaries inside and along the margins of albite-rich veins (Figs. 5G and 5H). We note that the long axis of the needles is, in most cases, perpendicular to the main foliation of the host. It is proposed here that the orientation of the principal compressive stress was parallel to the direction of vein amphibole needles during near-peak burial conditions (see also Moore et al. [2019] for another example). This stress orientation is kinematically compatible with the basal accretion process and ongoing nappe stacking on the interface (Richter et al., 2007). Additional reorientation and deformation occurred during duplex exhumation as shown by the S3 fabrics.

Assessment of the Fluid Budget

Here we evaluate whether external fluid input is needed to justify the great abundance of veins observed in the Infiernillo sequence. Our fluid production model predicts an average of ~9.4, 12.0, and 14.4 wt% of H_2O liberated from the blue-green schists, dark phyllites, and orange metasediments, respectively. Thus, to precipitate 0.45 vol% of albite and 6.85 vol% of quartz veins (not considering calcite; surface percent values of veins are shown in Table 2) from a rock volume of 100 m^3 (0.45 m^3 of albite and 6.85 m^3 of quartz veins), solubilities of ~50.2 wt% for quartz and ~3.3 wt% for albite are needed (for further explanation, see Appendix

2; note that albite is considered in the calculation only in the blue-green schists because it is volumetrically rather abundant in this rock type). In agreement with our results, experimental studies have demonstrated that at *P-T* conditions above 0.9 GPa and 500 °C and under pure H_2O compositions, albite solubilities in H_2O fluid are on the same order of magnitude as those calculated here (e.g., ~2.5 wt%; Shmulovich et al., 2001). However, quartz solubilities are still one order of magnitude lower compared to our results (e.g., ~1–4 wt%; Newton and Manning, 2000; Shmulovich et al., 2001).

It is known that chemical gradients may redistribute silica through diffusion mechanisms (Thompson, 1959; Korzhinskiĭ, 1970). This process has been considered of minor importance in terms of mass transport in regional metamorphic environments, where classical works have shown that solute diffusion through a standing fluid would take >200 yr to reach the same transport distance as via fluid advection, the latter process taking place in few years considering permeabilities as low as 10^{-20} m^2 (e.g., Fletcher and Hoffman, 1974; Rutter, 1976; Etheridge et al., 1984). On the other hand, several authors have proposed, based on $\delta^{18}O$ and $\delta^{13}C$, that fluid-hosted diffusion may enhance silica (and carbonate) elemental mobility, allowing the formation of calcite and quartz veins (Cartwright et al., 1994; Henry et al., 1996; Cartwright and Barnicoat, 1999). However, the lack of elemental depletion adjacent to the host-vein contact, identified only in few cases (Yardley, 1986; Cartwright and Barnicoat, 1999), suggests that silica mobility occurred through distances on the order of decimeters to meters under steady-state conditions (Cartwright and Buick, 2000). In addition, this process also requires large amounts of fluid (Etheridge et al., 1983). Because transient, near-lithostatic pore-fluid pressure conditions and fracturing likely occur in a time span ranging from hours to days (e.g., Husen and Kissling, 2001; Frank et al., 2015), it is difficult to envision how the great amounts of quartz veins in the studied locality may have formed via only diffusion-related processes. In addition, the Infiernillo exposures lack evidence indicating substantial internal silica redistribution (e.g., massive and abundant solution seams, silica content or paragenetic changes approaching the veins). Therefore, we propose here that external fluids rich in quartz and calcite components (see, e.g., Fig. 6) were injected into the system through strongly channelized pathways near peak burial conditions (e.g., Cartwright and Barnicoat, 1999; Miller et al., 2000; Breeding and Ague, 2002; Lewerentz et al., 2017; Jaeckel et al., 2018; Fig. 11). An external origin of CO_2 in the fluid phase infiltrating the studied vein sets is confirmed by the lack of calcite in the matrix material from all studied lithologies (e.g., Fig. 8D). The CO_2 required to form calcite veins may come from decarbonation reactions, which would take place at greater depths along the subduction channel than that of Infiernillo peak metamorphism (Cook-Kollars et al., 2014; Ague and Nicolescu, 2014; Menzel et al., 2020).

Nature and Mechanisms of Fluid-Rock Interaction Processes

Fluid release due to metamorphic dehydration reactions when crustal rocks enter the blueschist-eclogite facies transition (between 40 and 70 km depth, depending on the *P-T* gradient) is known to be responsible for very high pore-fluid pressure regions in the subduction environment (Audet et al., 2009; Fagereng and Diener, 2011; Saffer and Tobin, 2011). We have shown that the pervasive vein networks observed in Infiernillo rocks are the protracted result of (1) shallow prograde veining related to porosity collapse and early dehydration reactions along the interface before entering the slow-slip region (< 250 °C; Fig. 11), and (2) lower blueschist facies hydrofracturing due to external influx, as the relatively flat crustal dehydration pattern does not argue for massive local production in the 250–400 °C window (Figs. 10B, 11). By which physical mechanism did the external fluids enter the crustal sequence of Infiernillo, causing hydrofracturing on their way?

It has been proposed that fluids under near-lithostatic pressures can travel upward away from the reaction zone, either as "porosity waves" (Connolly, 1997) or along major sheared domains (Kawano et al., 2011; Angiboust et al., 2014). Heat may also be advected along with fluids, resulting in a local perturbation of the geothermal gradient (e.g., Vrolijk et al., 1988; Spinelli and Wang, 2008; Harris et al., 2013). Studies of low-frequency earthquakes have proposed that metamorphic fluids may be trapped due to permeability anisotropies, implying weakening of the fault (Audet et al., 2009; Peacock et al., 2011; Frank et al., 2015). According to this model, during slow-slip events, along-fault permeability increases due to the creation of an interconnected network of "reactivated" structures, resulting in high pore-fluid pressure pulses that travel updip through the subduction interface at velocities on the order of 1 km/day (Radiguet et al., 2011; Frank et al., 2015). Interestingly, most deep hydrofractures at the Infiernillo locality exhibit multiple stages of opening, as suggested by the presence of crack-seal bands (e.g., Ramsay, 1980) and sequential mineral precipitation events (e.g., Figs. 5B, 6D–6F). Based on textural and fabric relationships, we infer that previous vein networks represent preferential mechanical weaknesses that enable external infiltration (e.g., Bons et al., 2012; Frank et al., 2015). Once opened, the veins enable fast influx of high pore-fluid pulses, triggering further hydrofracturing, a drop of the fault zone friction coefficient, and ultimately the shearing of the metamorphic sequence (Fig. 11). It is commonly accepted that in active subduction systems, slow-slip events and episodic tremor would be triggered in such fluid-saturated environments, characterized by high ratios of P-wave to S-wave velocities (Vp/Vs) (Wang et al., 2006; Audet et al., 2009). This mechanism supports the idea that forces acting in the same direction of fluid motion, parallel to the subduction interface, may result in dilatational features (Shapiro et al., 2018). Nevertheless, the presence of (1) burial-related oblique (ptygmatic) veins cutting and being cut by veins oriented parallel to the main foliation and (2) amphibole needles oriented perpendicular to the vein margins suggests that the orientation of the least principal compressive stress (σ_3) must in fact be variable with time, switching between subparallel to subvertical on the subduction interface fault (e.g., Meneghini and Moore, 2007; Ujiie et al., 2018; Cerchiari et al., 2020). The apparent diversity of deformation patterns affecting the

rocks along the subduction interface can likely be reconciled considering the evolution of the stress regime at the seismic-cycle time scale (e.g., Magee and Zoback, 1993).

Last, we postulate that several distinct pulses contributed to the final state recorded in the exposure, as evidenced by crack-seal textures and cross-cutting relationships resulting from the studied hydrofracture events (e.g., Figs. 5B, 6D–6F; Ramsay, 1980; Bachmann et al., 2009; Cerchiari et al., 2020). To precisely evaluate the amount of material deposited after a single pulse event, further fluid-rock experimental work is needed to refine (1) our understanding of the kinetics of fluid precipitation in vein systems and (2) the quantification of the physico-chemical parameters acting during vein-filling processes. This information will help better constrain fluid transport dynamics in the episodic tremor region, and hence improve our understanding of the rheological properties of the plate interface as well as megathrust rupture nucleation processes.

CONCLUSIONS

Field and analytical results reveal that the Infiernillo sequence (central Chile) corresponds to a several-hundred-meter-thick stack of trench sediments and accreted oceanic material affected by multiple veining stages. Our investigation suggests that chemical and mineralogical differences in the protolith composition are the key factors controlling the millimeter- to centimeter-scale occurrence of interlayered blueschist and greenschist, instead of selective retrogression due to late fluid influx. Additionally, our observations and results show that most of the veins present at the Infiernillo locality were formed during prograde burial toward peak conditions, from the contribution of three likely sources: (1) fluids expelled during initial compaction, (2) fluids originated from metamorphic dehydration reactions, and (3) external deeply generated fluid sources. Based on our calculations and observations, we propose that near-lithostatic pore-pressure pulses supply the additional input of fluids necessary to justify the great amount of veins at the Infiernillo locality. These results shed light on fluid-rock interaction and overpressurized fluid mobility at the base of the seismogenic zone, as documented by seismological studies reporting high-Vp/Vs segments as well as episodic tremor and slip events.

ACKNOWLEDGMENTS

Thaïs Hyppolito is acknowledged for sharing her knowledge about local geology. Anne Verlaguet, Hugues Raimbourg, and James Connolly are also acknowledged for insightful discussions on fluid-rock metamorphic processes. Ralf Halama and two anonymous reviewers are warmly acknowledged for insightful comments. Mauricio Calderón, Francisco Fuentes, and the Earth Sciences department at Universidad Andrés Bello (Santiago, Chile) are thanked for their technical assistance. A.C. acknowledges the research grant provided by the Alexander von Humboldt Foundation for a post-doctoral fellowship at Ruhr-Universität Bochum. This work has been funded by an Initiative D'EXcellence (IDEX) grant 16C538 to S.A. The University of Granada is acknowledged for partial funding. Part of this work was also supported by the TelluS Program of CNRS/INSU. This is Institut de Physique du Globe de Paris contribution 4124.

Appendix 1. "Synthetic Minerals" Model

Theoretical end-member mineral compositions for the blue-green schist BS and GS compositions are: Ca-amphibole (relict hornblende), actinolite, albite, analcime (zeolite), montmorillonite, clinochlore (chlorite), muscovite, stilpnomelane, quartz, clinopyroxene (relict augite), iron oxide, and prehnite (e.g., Cho et al., 1986; Thompson and Humphris, 1977). The theoretical minerals considered for the dark phyllites and orange metasediments are: kaolinite, berthierine, montmorillonite, clinochlore, albite, quartz, dickite, illite, and stilpnomelane (e.g., Worden and Morad, 2003). Mineral proportions vary thorough the path from 0 to 250 °C (every 50 °C). The H_2O content in each step corresponds to the sum of the H_2O (in weight percent) in each mineral multiplied by its volume abundance (assuming mineral densities as selected for each type of rock). In addition, we considered the fluid contained in porosity, from which we fixed the values detailed in Figure 10A. Density values are as mentioned in the caption of Figure 10.

The next step is to sum thermodynamically calculated water released to the "synthetic minerals." Finally, the average between BS and GS compositions is considered as representative for the blue-green schists, together with compositions of the dark phyllites and orange metasediments. The mineral proportions considered and H_2O released are shown in Table S4 (footnote 1).

Appendix 2. Solubility Calculations

For solubility calculations, an initial volume of 100 m^3 is considered, where 6.85 vol% (6.85×10^6 cm^3) corresponds to quartz and 0.45 vol% (0.45×10^6 cm^3) to albite veins, giving 92.3 vol% (92.3×10^6 cm^3) of host-rock matrix, which is normalized to 100%. The next step is to multiply the volume values by density, which is calculated after the thermodynamic modeling considering the compositions of the blue-green schists, orange metasediments, and dark phyllites (~2.80 g/cm^3; see Table 2). The new values correspond to the mass of matrix, quartz, and albite in grams. Using the H_2O (in weight percent) values calculated after thermodynamic and "synthetic minerals" modeling, the mass of H_2O liberated from the matrix can be calculated by multiplying the weighted percentage fraction by the mass of rock of each of the three units (W_{Lib}, calculated from thermodynamic and "synthetical minerals" modeling). Finally, the solubility can be calculated by dividing the mass of quartz and/or albite by the mass of water liberated. The H_2O needed (W_{Ned}) is calculated multiplying the H_2O liberated by the mass of quartz present in the beach exposures and dividing by the mass of quartz that would precipitate from the fixed solubility value (0.3 wt% for quartz, extrapolated from Anderson and Burnham [1965]). To precipitate the amount of quartz present in veins (~17.8×10^6 g), ~59.4×10^8 g of water is necessary; in other words, 167 times more fluid than what has been produced by dehydration during burial must be released (W_{Ned}/W_{Lib}). Analogue calculations were made for albite but considering a solubility value of 0.25 wt% (extrapolated from Currie [1968]).

REFERENCES CITED

Ague, J.J., and Nicolescu, S., 2014, Carbon dioxide released from subduction zones by fluid-mediated reactions: Nature Geoscience, v. 7, p. 355–360, https://doi.org/10.1038/ngeo2143.

Aguirre, L., Hervé, F., and Godoy, E., 1972, Distribution of metamorphic facies in Chile—An outline: Krystalinikum, v. 9, p. 7–19.

Anderson, G.M., and Burnham, C.W., 1965, The solubility of quartz in super-critical water: American Journal of Science, v. 263, p. 494–511, https://doi.org/10.2475/ajs.263.6.494.

Angiboust, S., and Harlov, D., 2017, Ilmenite breakdown and rutile-titanite stability in metagranitoids: Natural observations and experimental results: American Mineralogist, v. 102, p. 1696–1708, https://doi.org/10.2138/am-2017-6064.

Angiboust, S., Pettke, T., De Hoog, J.C.M., Caron, B., and Oncken, O., 2014, Channelized fluid flow and eclogite-facies metasomatism along the subduction shear zone: Journal of Petrology, v. 55, p. 883–916, https://doi.org/10.1093/petrology/egu010.

Angiboust, S., Kirsch, J., Oncken, O., Glodny, J., Monié, P., and Rybacki, E., 2015, Probing the transition between seismically coupled and decoupled segments along an ancient subduction interface: Geochemistry Geophysics Geosystems, v. 16, p. 1905–1922, https://doi.org/10.1002/2015GC005776.

Angiboust, S., Cambeses, A., Hyppolito, T., Glodny, J., Monié, P., Calderón, M., and Juliani, C., 2018, A 100-my-long window onto mass-flow processes in the Patagonian Mesozoic subduction zone (Diego de Almagro Island, Chile): Geological Society of America Bulletin, v. 130, p. 1439–1456, https://doi.org/10.1130/B31891.1.

Audet, P., Bostock, M.G., Christensen, N.I., and Peacock, S.M., 2009, Seismic evidence for overpressured subducted oceanic crust and megathrust fault sealing: Nature, v. 457, p. 76–78, https://doi.org/10.1038/nature07650.

Bachmann, R., Oncken, O., Glodny, J., Seifert, W., Georgieva, V., and Sudo, M., 2009, Exposed plate interface in the European Alps reveals fabric styles and gradients related to an ancient seismogenic coupling zone: Journal of Geophysical Research, v. 114, B05402, https://doi.org/10.1029/2008JB005927.

Barrientos, X., and Selverstone, J., 1993, Infiltration vs. thermal overprinting of epidote blueschists, Ile de Groix, France: Geology, v. 21, p. 69–72, https://doi.org/10.1130/0091-7613(1993)021<0069:IVTOOE>2.3.CO;2.

Baziotis, I., and Mposkos, E., 2011, Origin of metabasites from upper tectonic unit of the Lavrion area (SE Attica, Greece): Geochemical implications for dual origin with distinct provenance of blueschist and greenschist's protoliths: Lithos, v. 126, p. 161–173, https://doi.org/10.1016/j.lithos.2011.07.014.

Bebout, G.E., 2007, Metamorphic chemical geodynamics of subduction zones: Earth and Planetary Science Letters, v. 260, p. 373–393, https://doi.org/10.1016/j.epsl.2007.05.050.

Bebout, G.E., and Barton, M.D., 1993, Metasomatism during subduction: Products and possible paths in the Catalina Schist, California: Chemical Geology, v. 108, p. 61–92, https://doi.org/10.1016/0009-2541(93)90318-D.

Bebout, G.E., and Penniston-Dorland, S.C., 2016, Fluid and mass transfer at subduction interfaces—The field metamorphic record: Lithos, v. 240, p. 228–258, https://doi.org/10.1016/j.lithos.2015.10.007.

Bons, P.D., 2001, The formation of large quartz veins by rapid ascent of fluids in mobile hydrofractures: Tectonophysics, v. 336, p. 1–17, https://doi.org/10.1016/S0040-1951(01)00090-7.

Bons, P.D., Elburg, M.A., and Gomez-Rivas, E., 2012, A review of the formation of tectonic veins and their microstructures: Journal of Structural Geology, v. 43, p. 33–62, https://doi.org/10.1016/j.jsg.2012.07.005.

Breeding, C.M., and Ague, J.J., 2002, Slab-derived fluids and quartz-vein formation in an accretionary prism, Otago Schist, New Zealand: Geology, v. 30, p. 499–502, https://doi.org/10.1130/0091-7613(2002)030<0499:SDFAQV>2.0.CO;2.

Bröcker, M., 1990, Blueschist-to-greenschist transition in metabasites from Tinos Island, Cyclades, Greece: Compositional control or fluid infiltration?: Lithos, v. 25, p. 25–39, https://doi.org/10.1016/0024-4937(90)90004-K.

Carlson, R.L., and Herrick, C.N., 1990, Densities and porosities in the oceanic crust and their variations with depth and age: Journal of Geophysical Research, v. 95, p. 9153–9170, https://doi.org/10.1029/JB095iB06p09153.

Cartwright, I., and Barnicoat, A.C., 1999, Stable isotope geochemistry of Alpine ophiolites: A window to ocean-floor hydrothermal alteration and constraints on fluid–rock interaction during high-pressure metamorphism: International Journal of Earth Sciences, v. 88, p. 219–235, https://doi.org/10.1007/s005310050261.

Cartwright, I., and Buick, I.S., 2000, Fluid generation, vein formation and the degree of fluid–rock interaction during decompression of high-pressure terranes: The Schistes Lustrés, Alpine Corsica, France: Journal of Metamorphic Geology, v. 18, p. 607–624, https://doi.org/10.1046/j.1525-1314.2000.00280.x.

Cartwright, I., Power, W.L., Oliver, N.H.S., Valenta, R.K., and McLatchie, G.S., 1994, Fluid migration and vein formation during deformation and greenschist facies metamorphism at Ormiston Gorge, central Australia: Journal of Metamorphic Geology, v. 12, p. 373–386, https://doi.org/10.1111/j.1525-1314.1994.tb00030.x.

Cerchiari, A., Remitti, F., Mittempergher, S., Festa, A., Lugli, F., and Cipriani, A., 2020, Cyclical variations of fluid sources and stress state in a shallow megathrust-zone mélange: Journal of the Geological Society, https://doi.org/10.1144/jgs2019-072 (in press).

Charrier, R., Ramos, V.A., Tapia, F., and Sagripanti, L., 2015, Tectono-stratigraphic evolution of the Andean Orogen between 31 and 37°S (Chile and Western Argentina), *in* Sepúlveda, S.A., Giambiagi, L.B., Moreiras, S.M., Pinto, L., Tunik, M., Hoke, G.D., and Farías, M., eds., Geodynamic Processes in the Andes of Central Chile and Argentina: Geological Society of London Special Publication 399, p. 13–61, https://doi.org/10.1144/SP399.20.

Cho, M., Liou, J.G., and Maruyama, S., 1986, Transition from the zeolite to prehnite-pumpellyite facies in the Karmutsen metabasites, Vancouver Island, British Columbia: Journal of Petrology, v. 27, p. 467–494, https://doi.org/10.1093/petrology/27.2.467.

Connolly, J.A.D., 1997, Devolatilization-generated fluid pressure and deformation-propagated fluid flow during prograde regional metamorphism: Journal of Geophysical Research, v. 102, p. 18,149–18,173, https://doi.org/10.1029/97JB00731.

Connolly, J.A.D., 2005, Computation of phase equilibria by linear programming: A tool for geodynamic modeling and its application to subduction zone decarbonation: Earth and Planetary Science Letters, v. 236, p. 524–541, https://doi.org/10.1016/j.epsl.2005.04.033.

Cook-Kollars, J., Bebout, G.E., Collins, N.C., Angiboust, S., and Agard, P., 2014, Subduction zone metamorphic pathway for deep carbon cycling: I. Evidence from HP/UHP metasedimentary rocks, Italian Alps: Chemical Geology, v. 386, p. 31–48, https://doi.org/10.1016/j.chemgeo.2014.07.013.

Coombs, D.S., 1960, Lower grade mineral facies in New Zealand, *in* Proceedings, 21st International Geological Congress, Part 13, p. 339–351.

Cox, S.F., and Etheridge, M.A., 1983, Crack-seal fibre growth mechanisms and their significance in the development of oriented layer silicate microstructures: Tectonophysics, v. 92, p. 147–170, https://doi.org/10.1016/0040-1951(83)90088-4.

Currie, K.L., 1968, On the solubility of albite in supercritical water in the range of 400 degrees to 600 degrees C and 750 to 3500 bars: American Journal of Science, v. 266, p. 321–341, https://doi.org/10.2475/ajs.266.5.321.

Dielforder, A., Vollstaedt, H., Vennemann, T., Berger, A., and Herwegh, M., 2015, Linking megathrust earthquakes to brittle deformation in a fossil accretionary complex: Nature Communications, v. 6, 7504, https://doi.org/10.1038/ncomms8504.

Dungan, M.A., Vance, J.A., and Blanchard, D.P., 1983, Geochemistry of the Shuksan greenschists and blueschists, North Cascades, Washington: Variably fractionated and altered metabasalts of oceanic affinity: Contributions to Mineralogy and Petrology, v. 82, p. 131–146, https://doi.org/10.1007/BF01166608.

Etheridge, M.A., Wall, V.J., and Vernon, R.H., 1983, The role of the fluid phase during regional metamorphism and deformation: Journal of Metamorphic Geology, v. 1, p. 205–226, https://doi.org/10.1111/j.1525-1314.1983.tb00272.x.

Etheridge, M.A., Wall, V.J., Cox, S.F., and Vernon, R.H., 1984, High fluid pressures during regional metamorphism and deformation: Implications for mass transport and deformation mechanisms: Journal of Geophysical Research, v. 89, p. 4344–4358, https://doi.org/10.1029/JB089iB06p04344.

Evans, B.W., 1990, Phase relations of epidote-blueschists: Lithos, v. 25, p. 3–23, https://doi.org/10.1016/0024-4937(90)90003-J.

Fagereng, Å., and Diener, J.F.A., 2011, Non-volcanic tremor and discontinuous slab dehydration: Geophysical Research Letters, v. 38, L15302, https://doi.org/10.1029/2011GL048214.

Fagereng, Å., and Toy, V.G., 2011, Geology of the earthquake source: An introduction, *in* Fagereng, Å., Toy, V.G., and Rowland, J.V., eds., Geology of the Earthquake Source: A Volume in Honour of Rick Sibson: Geological Society of London Special Publication 359, p. 1–16, https://doi.org/10.1144/SP359.1.

Fagereng, Å., Remitti, F., and Sibson, R.H., 2010, Shear veins observed within anisotropic fabric at high angles to the maximum compressive stress: Nature Geoscience, v. 3, p. 482–485, https://doi.org/10.1038/ngeo898.

Fisher, D.M., and Brantley, S.L., 1992, Models of quartz overgrowth and vein formation: Deformation and episodic fluid flow in an ancient subduction zone: Journal of Geophysical Research, v. 97, p. 20,043–20,061, https://doi.org/10.1029/92JB01582.

Fletcher, R.C., and Hofmann, A.W., 1974, Simple models of diffusion and combined diffusion-infiltration metasomatism, *in* Hoffman, A.W., Giletti, H.S., Yoder, H.S., Jr., and Yund, R.A., eds., Geochemical Transport and Kinetics: Carnegie Institution of Washington Publication 634, p. 243–259.

Frank, W.B., Shapiro, N.M., Husker, A.L., Kostoglodov, V., Bhat, H.S., and Campillo, M., 2015, Along-fault pore-pressure evolution during a slow-slip event in Guerrero, Mexico: Earth and Planetary Science Letters, v. 413, p. 135–143, https://doi.org/10.1016/j.epsl.2014.12.051.

Fyfe, W.S., Price, N.J., and Thompson, A.B., 1978, Fluids in the Earth's Crust: Their Significance in Metamorphic, Tectonic and Chemical Transport Processes: New York, Elsevier Scientific, Developments in Geochemistry, v. 1, 401 p.

García-Casco, A., 2007, Magmatic paragonite in trondhjemites from the Sierra del Convento mélange, Cuba: American Mineralogist, v. 92, p. 1232–1237, https://doi.org/10.2138/am.2007.2598.

Glodny, J., Lohrmann, J., Echtler, H., Gräfe, K., Seifert, W., Collao, S., and Figueroa, O., 2005, Internal dynamics of a paleoaccretionary wedge: Insights from combined isotope tectonochronology and sandbox modelling of the South-Central Chilean forearc: Earth and Planetary Science Letters, v. 231, p. 23–39, https://doi.org/10.1016/j.epsl.2004.12.014.

Halama, R., and Konrad-Schmolke, M., 2015, Retrograde metasomatic effects on phase assemblages in an interlayered blueschist-greenschist sequence (Coastal Cordillera, Chile): Lithos, v. 216, p. 31–47, https://doi.org/10.1016/j.lithos.2014.12.004.

Halama, R., Konrad-Schmolke, M., Sudo, M., Marschall, H.R., and Wiedenbeck, M., 2014, Effects of fluid–rock interaction on $^{40}Ar/^{39}Ar$ geochronology in high-pressure rocks (Sesia-Lanzo Zone, Western Alps): Geochimica et Cosmochimica Acta, v. 126, p. 475–494, https://doi.org/10.1016/j.gca.2013.10.023.

Harlow, G.E., and Sorensen, S.S., 2005, Jade (nephrite and jadeitite) and serpentinite: Metasomatic connections: International Geology Review, v. 47, p. 113–146, https://doi.org/10.2747/0020-6814.47.2.113.

Harris, R., Yamano, M., Kinoshita, M., Spinelli, G., Hamamoto, H., and Ashi, J., 2013, A synthesis of heat flow determinations and thermal modeling along the Nankai Trough, Japan: Journal of Geophysical Research: Solid Earth, v. 118, p. 2687–2702, https://doi.org/10.1002/jgrb.50230.

Henry, C., Burkhard, M., and Goffe, B., 1996, Evolution of syn-metamorphic veins and their wallrocks through a Western Alps transect: No evidence for large-scale fluid flow. Stable isotope, major- and trace-element systematics: Chemical Geology, v. 127, p. 81–109, https://doi.org/10.1016/0009-2541(95)00106-9.

Hervé, F., 1988, Late Paleozoic subduction and accretion in Southern Chile: Episodes, v. 11, p. 183–188, https://doi.org/10.18814/epiiugs/1988/v11i3/005.

Hervé, F., Kawashita, K., Munizaga, F., and Bassei, M., 1984, Rb-Sr isotopic ages from late Palaeozoic metamorphic rocks of central Chile: Journal of the Geological Society, v. 141, p. 877–884, https://doi.org/10.1144/gsjgs.141.5.0877.

Hervé, F., Calderón, M., Fanning, C.M., Pankhurst, R.J., and Godoy, E., 2013, Provenance variations in the Late Paleozoic accretionary complex of central Chile as indicated by detrital zircons: Gondwana Research, v. 23, p. 1122–1135, https://doi.org/10.1016/j.gr.2012.06.016.

Holland, T., and Powell, R., 1996, Thermodynamics of order-disorder in minerals: II. Symmetric formalism applied to solid solutions: The American Mineralogist, v. 81, p. 1425–1437, https://doi.org/10.2138/am-1996-11-1215.

Holland, T., and Powell, R., 2003, Activity-composition relations for phases in petrological calculations: An asymmetric multicomponent formulation: Contributions to Mineralogy and Petrology, v. 145, p. 492–501, https://doi.org/10.1007/s00410-003-0464-z.

Holland, T.J.B., and Powell, R., 1998, An internally consistent thermodynamic data set for phases of petrological interest: Journal of Metamorphic Geology, v. 16, p. 309–343, https://doi.org/10.1111/j.1525-1314.1998.00140.x.

Husen, S., and Kissling, E., 2001, Postseismic fluid flow after the large subduction earthquake of Antofagasta, Chile: Geology, v. 29, p. 847–850, https://doi.org/10.1130/0091-7613(2001)029<0847:PFFATL>2.0.CO;2.

Hyndman, R.D., 1988, Dipping seismic reflectors, electrically conductive zones, and trapped water in the crust over a subducting plate: Journal of Geophysical Research, v. 93, p. 13,391–13,405, https://doi.org/10.1029/JB093iB11p13391.

Hyppolito, T., Juliani, C., García-Casco, A., Meira, V.T., Bustamante, A., and Hervé, F., 2014a, The nature of the Palaeozoic oceanic basin at the southwestern margin of Gondwana and implications for the origin of the Chilenia terrane (Pichilemu region, central Chile): International Geology Review, v. 56, p. 1097–1121, https://doi.org/10.1080/00206814.2014.919612.

Hyppolito, T., García-Casco, A., Juliani, C., Meira, V.T., and Hall, C., 2014b, Late Paleozoic onset of subduction and exhumation at the western margin of Gondwana (Chilenia Terrane): Counterclockwise P-T paths and timing of metamorphism of deep-seated garnet-mica schist and amphibolite of Punta Sirena, Coastal Accretionary Complex, central Chile (34° S): Lithos, v. 206, p. 409–434, https://doi.org/10.1016/j.lithos.2014.07.023.

Hyppolito, T.N., 2014, Metamorfismo y evolucion tectonica del cinturon pareado Permo-Carbonifero en la region de Pichilemu, cordillera de la costa de Chile central [Ph.D. thesis]: Sao Paulo, Granada, Universidade de Sao Paulo and Universidad de Granada, 358 p.

Jaeckel, K., Bebout, G.E., and Angiboust, S., 2018, Deformation-enhanced fluid and mass transfer along Western and Central Alps paleo-subduction interfaces: Significance for carbon cycling models: Geosphere, v. 14, p. 2355–2375, https://doi.org/10.1130/GES01587.1.

Kawano, S., Katayama, I., and Okazaki, K., 2011, Permeability anisotropy of serpentinite and fluid pathways in a subduction zone: Geology, v. 39, p. 939–942, https://doi.org/10.1130/G32173.1.

Korzhinskiĭ, D.S., 1970, Theory of Metasomatic Zoning [translated from Russian by Jean Agrell]: London, Clarendon Press, 162 p.

Leake, B.E., Woolley, A.R., Arps, C.E.S., Birch, W.D., Gilbert, M.C., Grice, J.D., Hawthorne, F.C., Kato, A., Kisch, H.J., Krivovichev, V.G., Linthout, K., Laird, J., Mandarino, J., Maresch, W.V., Nickel, E.H., Rock, N.M.S., Schumacher, J.C., Smith, D.C., Stephenson, N.C.N., Ungaretti, L., Whittaker, E.J.W., and Youzhi, G., 1997, Nomenclature of amphiboles: Report of the Subcommittee on Amphiboles of the International Mineralogical Association Commission on New Minerals and Mineral Names: Mineralogical Magazine, v. 61, p. 295–310, https://doi.org/10.1180/minmag.1997.061.405.13.

Lewerentz, A., Skelton, A.D., Linde, J.K., Nilsson, J., Möller, C., Crill, P.M., and Spicuzza, M.J., 2017, On the association between veining and index mineral distributions in Barrow's metamorphic zones, Glen Esk, Scotland: Journal of Petrology, v. 58, p. 885–907, https://doi.org/10.1093/petrology/egx039.

Liou, J.G., 1971, Analcime equilibria: Lithos, v. 4, p. 389–402, https://doi.org/10.1016/0024-4937(71)90122-8.

Lucassen, F., Trumbull, R., Franz, G., Creixell, C., Vásquez, P., Romer, R.L., and Figueroa, O., 2004, Distinguishing crustal recycling and juvenile additions at active continental margins: The Paleozoic to recent compositional evolution of the Chilean Pacific margin (36–41 °S): Journal of South American Earth Sciences, v. 17, p. 103–119, https://doi.org/10.1016/j.jsames.2004.04.002.

Magara, K., 1980, Comparison of porosity-depth relationships of shale and sandstone: Journal of Petroleum Geology, v. 3, p. 175–185, https://doi.org/10.1111/j.1747-5457.1980.tb00981.x.

Magee, M.E., and Zoback, M.D., 1993, Evidence for a weak interplate thrust fault along the northern Japan subduction zone and implications for the mechanics of thrust faulting and fluid expulsion: Geology, v. 21, p. 809–812, https://doi.org/10.1130/0091-7613(1993)021<0809:EFAWIT>2.3.CO;2.

Massonne, H.-J., and Willner, A.P., 2008, Phase relations and dehydration behaviour of psammopelite and mid-ocean ridge basalt at very-low-grade to low-grade metamorphic conditions: European Journal of Mineralogy, v. 20, p. 867–879, https://doi.org/10.1127/0935-1221/2008/0020-1871.

Meneghini, F., and Moore, J.C., 2007, Deformation and hydrofracture in a subduction thrust at seismogenic depths: The Rodeo Cove thrust zone, Marin Headlands, California: Geological Society of America Bulletin, v. 119, p. 174–183, https://doi.org/10.1130/B25807.1.

Menzel, M.D., Garrido, C.J., and Sánchez-Vizcaíno, V.L., 2020, Fluid-mediated carbon release from serpentinite-hosted carbonates during dehydration of antigorite-serpentinite in subduction zones: Earth and Planetary Science Letters, v. 531, 115964, https://doi.org/10.1016/j.epsl.2019.115964.

Miller, J.A., Buick, I.S., and Cartwright, I., 2000, Textural implications of high-pressure fluid flow controlled by pre-subduction deformation and alteration patterns: Journal of Geochemical Exploration, v. 69, p. 551–555, https://doi.org/10.1016/S0375-6742(00)00036-4.

Moore, J., Beinlich, A., Austrheim, H., and Putnis, A., 2019, Stress orientation–dependent reactions during metamorphism: Geology, v. 47, p. 151–154, https://doi.org/10.1130/G45632.1.

Moore, J.C., Shipley, T.H., Goldberg, D., Ogawa, Y., Filice, F., Fisher, A., Jurado, M.-J., Moore, G.F., Rabaute, A., Yin, H., Zwart, G., Brückmann, W., Henry, P., Ashi, J., Blum, P., Meyer, A., Housen, B., Kastner, M., Labaume, P., Laier, T., Leitch, E.C., Maltman, A.J., Peacock, S., Steiger, T.H., Tobin, H.J., Underwood, M.B., Xu, Y., and Zheng, Y., 1995, Abnormal fluid pressures and fault-zone dilation in the Barbados accretionary prism: Evidence from logging while drilling: Geology, v. 23, p. 605–608, https://doi.org/10.1130/0091-7613(1995)023<0605:AFPAFZ>2.3.CO;2.

Newton, R.C., and Manning, C.E., 2000, Quartz solubility in H_2O-NaCl and H_2O-CO_2 solutions at deep crust–upper mantle pressures and temperatures: 2–15 kbar and 500–900 °C: Geochimica et Cosmochimica Acta, v. 64, p. 2993–3005, https://doi.org/10.1016/S0016-7037(00)00402-6.

Obara, K., 2002, Nonvolcanic deep tremor associated with subduction in southwest Japan: Science, v. 296, p. 1679–1681, https://doi.org/10.1126/science.1070378.

Owen, C., 1989, Magmatic differentiation and alteration in isofacial greenschists and blueschists, Shuksan Suite, Washington: Statistical analysis of major-element variation: Journal of Petrology, v. 30, p. 739–761, https://doi.org/10.1093/petrology/30.3.739.

Palin, R.M., and White, R.W., 2016, Emergence of blueschists on Earth linked to secular changes in oceanic crust composition: Nature Geoscience, v. 9, p. 60–64, https://doi.org/10.1038/ngeo2605.

Peacock, S.M., 1993, The importance of blueschist → eclogite dehydration reactions in subducting oceanic crust: Geological Society of America Bulletin, v. 105, p. 684–694, https://doi.org/10.1130/0016-7606(1993)105<0684:TIOBED>2.3.CO;2.

Peacock, S.M., Wang, K., and McMahon, A.M., 2002, Thermal structure and metamorphism of subducting oceanic crust: Insight into Cascadia intraslab earthquakes, *in* Kirby, S., Wang, K., and Dunlop. S., eds., The Cascadia Subduction Zone and Related Subduction Systems: Seismic Structure, Intraslab Earthquakes and Processes, and Earthquake Hazards: Geological Survey of Canada Open File 4350, p. 123–126, https://doi.org/10.4095/222536.

Peacock, S.M., Christensen, N.I., Bostock, M.G., and Audet, P., 2011, High pore pressures and porosity at 35 km depth in the Cascadia subduction zone: Geology, v. 39, p. 471–474, https://doi.org/10.1130/G31649.1.

Pearce, J.A., 1996, A user's guide to basalt discrimination diagrams, *in* Wyman, D.A., ed., Trace Element Geochemistry of Volcanic Rocks: Applications for Massive Sulphide Exploration: Geological Association of Canada Short Course Notes 12, p. 79–113.

Pearce, J.A., 2008, Geochemical fingerprinting of oceanic basalts with applications to ophiolite classification and the search

for Archean oceanic crust: Lithos, v. 100, p. 14–48, https://doi.org/10.1016/j.lithos.2007.06.016.
Peng, Z., and Gomberg, J., 2010, An integrated perspective of the continuum between earthquakes and slow-slip phenomena: Nature Geoscience, v. 3, p. 599–607, https://doi.org/10.1038/ngeo940.
Philippot, P., and Selverstone, J., 1991, Trace-element-rich brines in eclogitic veins: Implications for fluid composition and transport during subduction: Contributions to Mineralogy and Petrology, v. 106, p. 417–430, https://doi.org/10.1007/BF00321985.
Powell, R., and Holland, T., 1999, Relating formulations of the thermodynamics of mineral solid solutions: Activity modelling of pyroxenes, amphiboles, and micas: The American Mineralogist, v. 84, p. 1–14, https://doi.org/10.2138/am-1999-1-201.
Radiguet, M., Cotton, F., Vergnolle, M., Campillo, M., Valette, B., Kostoglodov, V., and Cotte, N., 2011, Spatial and temporal evolution of a long term slow slip event: The 2006 Guerrero Slow Slip Event: Geophysical Journal International, v. 184, p. 816–828, https://doi.org/10.1111/j.1365-246X.2010.04866.x.
Raimbourg, H., Famin, V., Palazzin, G., Mayoux, M., Jolivet, L., Ramboz, C., and Yamaguchi, A., 2018, Fluid properties and dynamics along the seismogenic plate interface: Geosphere, v. 14, p. 469–491, https://doi.org/10.1130/GES01504.1.
Ramos, V.A., 1988, Late Proterozoic–early Paleozoic of South America: A collisional history: Episodes, v. 11, p. 168–174, https://doi.org/10.18814/epiiugs/1988/v11i3/003.
Ramsay, J.G., 1980, The crack-seal mechanism of rock deformation: Nature, v. 284, p. 135–139, https://doi.org/10.1038/284135a0.
Richter, P.P., Ring, U., Willner, A.P., and Leiss, B., 2007, Structural contacts in subduction complexes and their tectonic significance: The Late Palaeozoic coastal accretionary wedge of central Chile: Journal of the Geological Society, v. 164, p. 203–214, https://doi.org/10.1144/0016-76492005-181.
Rutter, E.H., 1976, A discussion on natural strain and geological structure—The kinetics of rock deformation by pressure solution: Philosophical Transactions of the Royal Society of London: Series A, Mathematical and Physical Sciences, v. 283, p. 203–219, https://doi.org/10.1098/rsta.1976.0079.
Saffer, D.M., and Tobin, H.J., 2011, Hydrogeology and mechanics of subduction zone forearcs: Fluid flow and pore pressure: Annual Review of Earth and Planetary Sciences, v. 39, p. 157–186, https://doi.org/10.1146/annurev-earth-040610-133408.
Scambelluri, M., and Philippot, P., 2001, Deep fluids in subduction zones: Lithos, v. 55, p. 213–227, https://doi.org/10.1016/S0024-4937(00)00046-3.
Shapiro, N.M., Campillo, M., Kaminski, E., Vilotte, J.-P., and Jaupart, C., 2018, Low-frequency earthquakes and pore pressure transients in subduction zones: Geophysical Research Letters, v. 45, p. 11,083–11,094, https://doi.org/10.1029/2018GL079893.
Shmulovich, K., Graham, C., and Yardley, B., 2001, Quartz, albite and diopside solubilities in H_2O-NaCl and H_2O-CO_2 fluids at 0.5–0.9 GPa: Contributions to Mineralogy and Petrology, v. 141, p. 95–108, https://doi.org/10.1007/s004100000224.
Sibson, R.H., 2013, Stress switching in subduction forearcs: Implications for overpressure containment and strength cycling on megathrusts: Tectonophysics, v. 600, p. 142–152, https://doi.org/10.1016/j.tecto.2013.02.035.
Spandler, C., and Hermann, J., 2006, High-pressure veins in eclogite from New Caledonia and their significance for fluid migration in subduction zones: Lithos, v. 89, p. 135–153, https://doi.org/10.1016/j.lithos.2005.12.003.
Spear, F.S., 1993, Metamorphic Phase Equilibria and Pressure-Temperature-Time Paths: Washington, D.C., Mineralogical Society of America, 799 p.
Spinelli, G.A., and Wang, K., 2008, Effects of fluid circulation in subducting crust on Nankai margin seismogenic zone temperatures: Geology, v. 36, p. 887–890, https://doi.org/10.1130/G25145A.1.
Thompson, G., and Humphris, S.E., 1977, Seawater-rock interactions in the oceanic basement, *in* Paquet, H., and Tardy, Y., eds., Proceedings of the 2nd International Symposium on Water-Rock Interaction: Strasbourg, France, p. 13–18.
Thompson, J.B., 1959, Local equilibrium in metasomatic processes, *in* Abelson, P.H., eds., Researches in Geochemistry, Volume 1: New York, John Wiley, p. 427–457.
Torres-Roldán, R.L., Garcia-Casco, A., and Garcia-Sanchez, P.A., 2000, CSpace: An integrated workplace for the graphical and algebraic analysis of phase assemblages on 32-bit Wintel platforms: Computers & Geosciences, v. 26, p. 779–793, https://doi.org/10.1016/S0098-3004(00)00006-6.
Ujiie, K., Saishu, H., Fagereng, Å., Nishiyama, N., Otsubo, M., Masuyama, H., and Kagi, H., 2018, An explanation of episodic tremor and slow slip constrained by crack-seal veins and viscous shear in subduction mélange: Geophysical Research Letters, v. 45, p. 5371–5379, https://doi.org/10.1029/2018GL078374.
Vitale Brovarone, A., Alard, O., Beyssac, O., Martin, L., and Picatto, M., 2014, Lawsonite metasomatism and trace element recycling in subduction zones: Journal of Metamorphic Geology, v. 32, p. 489–514, https://doi.org/10.1111/jmg.12074.
Vrolijk, P., Myers, G., and Moore, J.C., 1988, Warm fluid migration along tectonic melanges in the Kodiak Accretionary Complex, Alaska: Journal of Geophysical Research, v. 93, p. 10,313–10,324, https://doi.org/10.1029/JB093iB09p10313.
Wang, Z., Zhao, D., Mishra, O.P., and Yamada, A., 2006, Structural heterogeneity and its implications for the low frequency tremors in Southwest Japan: Earth and Planetary Science Letters, v. 251, p. 66–78, https://doi.org/10.1016/j.epsl.2006.08.025.
Whitmarsh, R.B., 1978, Seismic refraction studies of the upper igneous crust in the North Atlantic and porosity estimates for Layer 2: Earth and Planetary Science Letters, v. 37, p. 451–464, https://doi.org/10.1016/0012-821X(78)90061-4.
Whitney, D.L., and Evans, B.W., 2010, Abbreviations for names of rock-forming minerals: The American Mineralogist, v. 95, p. 185–187, https://doi.org/10.2138/am.2010.3371.
Willner, A.P., 2005, Pressure-temperature evolution of a Late Palaeozoic paired metamorphic belt in north-central Chile (34°–35°30′S): Journal of Petrology, v. 46, p. 1805–1833, https://doi.org/10.1093/petrology/egi035.
Willner, A.P., Thomson, S.N., Kröner, A., Wartho, J.-A., Wijbrans, J.R., and Hervé, F., 2005, Time markers for the evolution and exhumation history of a Late Palaeozoic paired metamorphic belt in north-central Chile (34°–35°30′S): Journal of Petrology, v. 46, p. 1835–1858, https://doi.org/10.1093/petrology/egi036.
Willner, A.P., Gerdes, A., and Massonne, H.J., 2008, History of crustal growth and recycling at the Pacific convergent margin of South America at latitudes 29°–36° S revealed by a U-Pb and Lu-Hf isotope study of detrital zircon from late Paleozoic accretionary systems: Chemical Geology, v. 253, p. 114–129, https://doi.org/10.1016/j.chemgeo.2008.04.016.
Willner, A.P., Maresch, W.V., Massonne, H.J., Sandritter, K., and Willner, G., 2016, Metamorphic evolution of blueschists, greenschists, and metagreywackes in the Cretaceous Mt. Hibernia Complex (SE Jamaica): European Journal of Mineralogy, v. 28, p. 1059–1078, https://doi.org/10.1127/ejm/2016/0028-2561.
Winchester, J.A., and Floyd, P.A., 1977, Geochemical discrimination of different magma series and their differentiation products using immobile elements: Chemical Geology, v. 20, p. 325–343, https://doi.org/10.1016/0009-2541(77)90057-2.
Worden, R.H., and Morad, S., 2003, Clay minerals in sandstones: Controls on formation, distribution and evolution, *in* Worden, R.H., and Morad, S., eds., Clay Mineral Cements in Sandstones: International Association of Sedimentologists Special Publication 34, p. 3–42, https://doi.org/10.1002/9781444304336.ch1.
Yardley, B.W.D., 1986, Fluid migration and veining in the Connemara Schists, Ireland, *in* Walther, J.V., and Wood, B.J., eds., Fluid-Rock Interactions during Metamorphism: Advances in Physical Geochemistry, v. 5: New York, Springer, p. 109–131, https://doi.org/10.1007/978-1-4612-4896-5_5.
Zack, T., and John, T., 2007, An evaluation of reactive fluid flow and trace element mobility in subducting slabs: Chemical Geology, v. 239, p. 199–216, https://doi.org/10.1016/j.chemgeo.2006.10.020.